Location-based Real-time Utilization of Intelligent Reflective Surfaces for mmWave Communication and Sensing in Full-Immersive Multiuser VR

Filip Lemic[1], *Jalal Jalali*[2], *Gerard Calvo Bartra*[1], *Alejandro Amat*[1], *Jakob Struye*[2], *Jeroen Famaey*[2], *Xavier Costa Perez*[134]

[1]i2Cat Foundation, Spain
[2]University of Antwerp - imec, Belgiun
[3]NEC Labs Europe GmbH, Germany
[4]ICREA, Spain

Contents

Abstract

The rapid progression of high-speed communication and computing technologies is ushering in an era where various user platforms coexist, facilitating deeper interactions in fully immersive virtual worlds. Advancements in technologies like Virtual Reality (VR) and high-frequency wireless communication networks, particularly in millimeter Wave (mmWave) bands, are paving the way for next-generation visualization platforms. These systems will empower users to navigate virtual environments seamlessly, receiving high-quality, real-time content via mmWave communication networks.

In this landscape, Joint Communication and Sensing (JCAS) emerges as a concept within 6G research on wireless communications. It leverages existing wireless communication infrastructures, such as mobile networks and WiFi, for both data transmission and sensing purposes. By utilizing wireless signals as illuminators and analyzing their reflections from users and objects, JCAS enhances situational awareness and enables functionalities like object detection and position estimation.

To address coverage challenges in mmWave networks while ensuring energy efficiency, Intelligent Reflective Surfaces (IRSs) are proposed as a potential solution. These surfaces, also known as Reconfigurable Intelligent Surfaces (RISs) or Software-Defined Metasurfaces (SDMs), consist of passive elements capable of dynamically adjusting electromagnetic wave phases. Strategically deploying IRS elements in wireless environments enhances signal strength, reduces path loss, and optimizes overall communication performance. However, the comprehensive evaluation of IRS deployment remains relatively unexplored. Given the impracticality of field experiments, computer simulations offer a viable means to assess IRS performance. In our study, we introduce a novel end-to-end simulation framework, based on the ns-3 simulator, aimed at optimizing IRS deployment for maximizing throughput and Signal-to-Noise Ratio (SNR) for each user location in a VR context. By simulating scenarios with and without IRS we demonstrate the effectiveness of IRS in supporting wireless communications for the next generation of VR platforms with multiple user coexistence.

1 Introduction

Virtual Reality (VR) is anticipated to transform our digital interactions in various domains, such as healthcare, tourism, education, entertainment, and occupational safety [29]. The advancement of VR relies on enhancing the quality of video content presented to VR users [9] and enabling collaborative multi-user experiences, where users can interact and cooperate within the virtual realm [4]. VR systems are poised to accommodate multiple fully-immersed users who can freely navigate their Virtual Experiences (VEs) in an indoor environment.

Advanced Machine Learning (ML)-enabled wireless communication networks will be essential, primarily operating in the millimeter Wave (mmWave) frequency band, spanning from 30 to 300 GHz [22]. These networks must offer highly directional transmission and reception capabilities to ensure seamless real-time delivery of high-quality video content to mobile VR users [22]. These directional mmWave beams are also expected to continuously track users' movements to maintain Line-of-Sight (LoS) connectivity, thus optimizing video quality. Simultaneously, the concept of ML-based redirected walking is being explored to prevent collisions among co-located users and between users and the boundaries of confined VR environments [4]. This approach allows VR users to move freely within the virtual realms while discreetly guiding them within the physical setups to avoid collisions, enhancing the overall immersion in the VEs.

The interactive multi-user VE envisions truthfully reproducing the actions of one user in the VEs of the other, potentially collocated users. Such interaction should be reproduced within the motion-to-photon latency of less than 20 ms to avoid causing nausea to the users [39]. Such motion capturing is traditionally performed using cameras strategically positioned in the environment [27]. However, such approaches by-design do not guarantee privacy preservation and induce significant delays due to cross-layer information collection and image processing overheads. More recently, high-frequency JCAS approaches have gained traction, in which the same communication wavefront is envisioned to be utilized for both tracking of the users and high throughput communication with them [47]. At the same time, passive sensing in the form of mmWave radar is envisaged to be employed for more advanced sensing tasks such as motion recognition or 3-Dimensional (3D) pose estimation [49].

In full-immersive VR applications, maintaining stable throughput is of prime importance for maintaining the users' Quality of Service (QoS) throughout their VEs. At the same time, active JCAS sensing tasks require the maximization of the Signal-to-Noise Ratio (SNR) of the communication wavefront for accuracy maximization [47]. These challenging requirements cannot be achieved with existing mmWave hardware such as IEEE 802.11ad/ay Access Points (APs), primarily due to the low number of antenna elements in the practical realization of mmWave transceivers, causing unequal coverage in the deployment environment, as will be demonstrated in the paper. An additional challenge comes from the fact that LoS communication with the users might be interrupted due to the presence of multiple users in the deployment environment, causing significant throughput and SNR degradation.

To enable cost-effective indoor VEs, the deployment of Intelligent Reflective Surfaces (IRSs) on the walls as a function of users' trajectory is a potential solution [9]. An IRS consists of large arrays of passive reflecting elements on a reconfigurable planar surface. These elements can independently modify the phase of an incoming signal before reflecting it towards its intended receiver. The IRS can be a boon for users experiencing significant path loss or blockage on the direct link, especially when primarily operating in the millimeter Wave (mmWave) frequency band, as the IRS creates additional propagation pathways | namely, reflected channels [44]. Moreover, the IRS offers added degrees of freedom through the phase shifts of the reflective elements, which can be harnessed to minimize interference [46, 15]. It is also worth noting that IRSs are envisioned to be manufactured as passive, cheap, and flexible entities adaptable for indoor VR streaming setups, as they could be used as "soft" environmental boundaries [19].

1.1 Contributions

In this Chapter, we consider an IRS-enabled multiuser mmWave VR environment, where the IRS is deployed on one of the walls, and a multi-antenna AP transmits data to a set of single-antenna Head Mounted Devices (HMDs) via the IRS. Specifically, we maximize the aggregate data rate of all HMDs by optimizing the location of the IRS, beamforming, phase shifts, and radiation patterns as a function of VR users' trajectory (modeled using redirected walking) in a confined indoor environment. For the considered full-immersive VR scenario, we study a novel IRS location optimization, where a multi-antenna AP transmits information symbols to a set of single-antenna HMDs. In particular, a resource allocation algorithm is designed to maximize the system's sum data-rate subject to peak transmit power feasibility and QoS constraints. The formulated problem is non-convex, thus we employ Alternative Optimization (AO) algorithm, segmenting the main optimization problem into four distinct sub-problems, in which each sub-problem is optimally solved. For the first sub-problem, i.e., the active beamforming at the AP, the Maximum-Ratio Transmission (MRT) is proved to be the optimal AP beamformer. In the second sub-problem, a closed-form optimal solution is obtained for the IRS phase shifts design using quadratic transformation. A global optimization of the IRS's placement is carried out in the third sub-problem based on a first-order derivative of the objective function. Finally, the optimal radiation pattern is determined in a closed-form format based on the monotonicity of the transformed objective function. The simulation results indicate that IRS with passive beamforming and location-based IRS placement, combined with an optimal beamforming at the AP, can achieve improved data-rates compared to a number of baseline schemes.

1.2 Structure

The structure of this paper is as follows. Section 2 provides an overview of related works and efforts. In Section 3, we describe the adopted system model and present a mathematical characterization of the channel for IRS and its optimal location. Section 4 describes our simulation methodology and outlines how well our approach performs in simulation. Finally, Section 5 concludes the Chapter.

2 Background, State-of-the-Art, and Challenges

2.1 Communication Challenges in VR

Forthcoming VR systems are envisioned to host multiple users simultaneously, engaging them in interactive VEs in which one user's actions influence the VE of other users, who may be co-located or remote. An additional goal is to sustain seamless immersion in VEs while ensuring uninhibited user movement within a tracking area, devoid of collisions with obstructions, environmental confines, or fellow users [42].

The prospective ability to facilitate the engagement of numerous users within interactive VEs will rely on advanced high-frequency wireless networks primarily operating in the mmWave spectrum, spanning from 30 to 300 GHz [11]. Given the high path loss when using these frequencies, it is paramount that APs and HMDs focus their energy towards each other, transmitting and receiving highly directionally, through a process called *beamforming* [31, 45]. This way, high-quality VR content can be delivered consistently and in real-time over high-gain links. In the VR scenario, directional mmWave beams should dynamically track users' movements during transmission, preserving LoS connections [39]. Additionally, Redirected Walking (RDW) will be harnessed to avert physical clashes between users and VR setup boundaries or collocated users, allowing them to explore VE freely while subtly adjusting their paths to prevent collisions, thereby enhancing the sense of immersion [30].

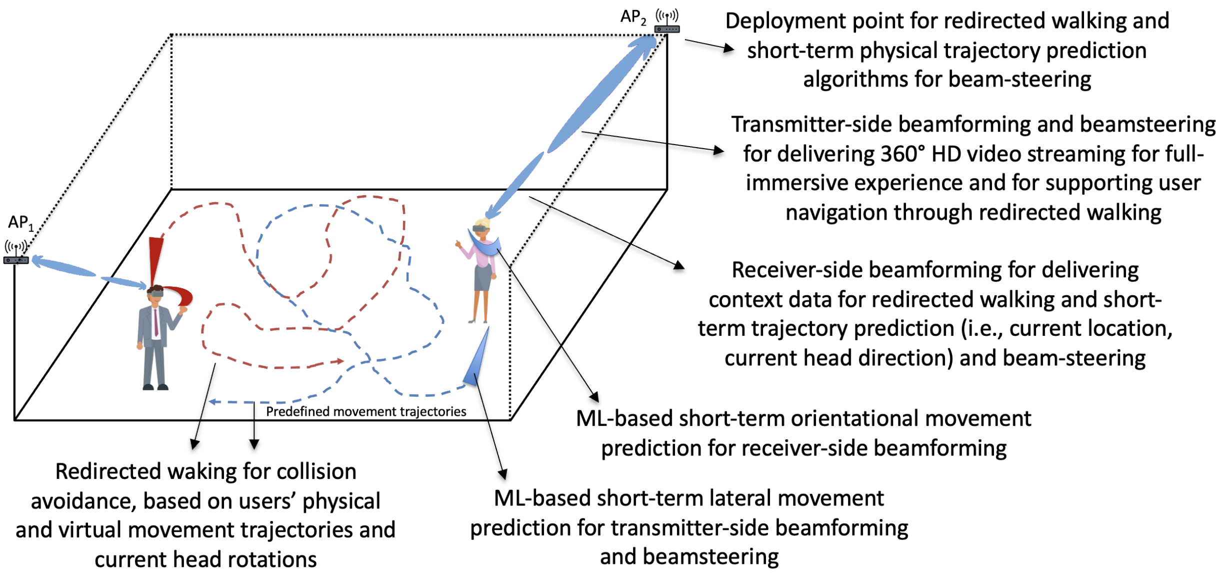

Figure 1: Full-immersive multiuser virtual reality with redirected walking [22]

Accurate short-term prediction of users' movements, both laterally and orientationally, are needed to ensure a convincing experience on several fronts. This enables not only accurate generation of content and proactive RDW [22], but also successful beamforming at both AP and HMD, as motion may be too sudden to allow for reactive beamforming [50]. To cater to this requirement, adaptable coverage proves invaluable for receiver-side beamforming on an HMD, as the slightest misalignment in beam orientation can notably impact the SNR [1]. Thus, a flexible beam stretching in the direction of HMD rotation can offer consistently high gain, essential for uninterrupted content delivery [39]. This strategy guarantees that user motion is promptly portrayed on-screen. Ideally this should happen within the 20 ms *motion-to-photon* latency bound, which is the maximal delay between a user's movement and the updated visual response they see on the screen that does not cause discomfort [11]. The above requirements highlight the necessity of maintaining stable communication coverage across an entire deployment environment. This is explored in details in this work, and addressed through the location-based utilization of IRS. A high-level system summary based on the above text is depicted in Figure 1.

A common method to enhance immersion in VEs involves directly mirroring users' physical movements within the VEs [12]. However, this approach typically confines users to limited tracking spaces, reducing overall immersion. To tackle this limitation, researchers have proposed diverse virtual locomotion techniques to facilitate movement across expansive VEs, even within confined tracking areas.

Leading-edge techniques leverage gestures resembling walking (e.g., walking-in-place), which have been demonstrated to create a convincing sensation of walking [38]. This effectiveness stems from studies in perception psychology revealing that visual input often overrides proprioception (sensing the body's position, movement, and actions) and vestibular sensations (related to balance and motion) when they conflict [10]. Essentially, humans excel at estimating their momentary direction of motion but struggle to perceive their exact paths of travel [18].

In VEs, this means users instinctively adjust for minor inconsistencies during locomotion, particularly when visual, proprioceptive, and vestibular cues differ. This enables imperceptible redirections using visual cues provided by VEs, a characteristic feature of RDW. RDW employs curvature gains (rotations of the virtual scene), translational gains (altering linear movements to change perceived distances traveled), and rotational gains (adding extra rotations to the user's existing rotation). Comprehensive discussions on the mathematical formulations of these gains, their perceptual thresholds, and experimental validations are available in prior studies [38, 37]. Notably, research indicates that VR users adjust their movement speeds in response to significant translational gains, even when these gains are not consciously perceivable.

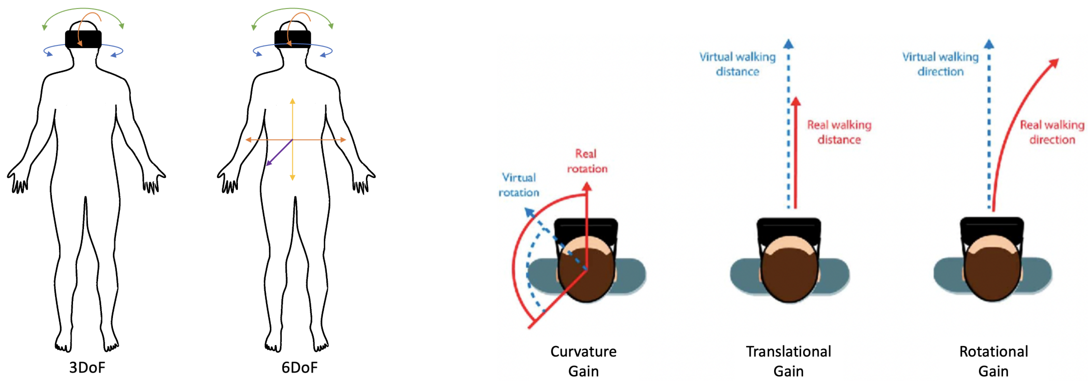

(a) 3DoF vs. 6DoF

(b) Redirected walking concepts [30]

Figure 2: Main concepts of redirected walking enabled through 6DoF non-tethered wireless HMDs [42]

2.2 Intelligent Reflective Surfaces

IRSs are envisioned to become a key enabling technology for next-generation mobile systems, such as beyond-5G/6G. An IRS consists of an array of sub-wavelength unit cells that can alter the electromagnetic (EM) response of the impinging radio-frequency (RF) signals in a nearly passive way. Indeed, IRSs can dynamically re-focus the received EM waves towards desired directions in space by suitably configuring the scattering properties of each unit cell. This ability unlocks new possibilities and opens up a new paradigm of the wireless environment, which has been treated as an optimization constraint in conventional systems, but can now be considered as a variable to be optimized, creating the so-called Smart Radio Environment. For example, when an obstacle hinders the LoS between the transmitter and the receiver, an IRS device strategically deployed can alleviate this problem via (passive) beamforming so as to effectively create a virtual LoS, which guarantees favorable signal propagation conditions. This can be achieved, for instance, by suitably designing the re-configurable phase shift provided by each unit cell to receive wireless signals such that the reflected signals may interfere constructively towards the desired direction and destructively elsewhere.

Prior research has underscored the advantages of integrating IRSs into traditional multi-user wireless communication frameworks [5, 15, 8, 51]. For instance, Chaccour *et al.* demonstrated that the IRS can enhance both the sum data-rate and the reliability of data transfer in VR contexts [8]. Jalali *et al.* delved into the IRS design for energy efficiency and admission control maximization for Internet of Things (IoT) users with short packet lengths [15]. Besser *et al.* introduced a phase hopping algorithm tailored for IRS-supported systems to elevate data transfer reliability

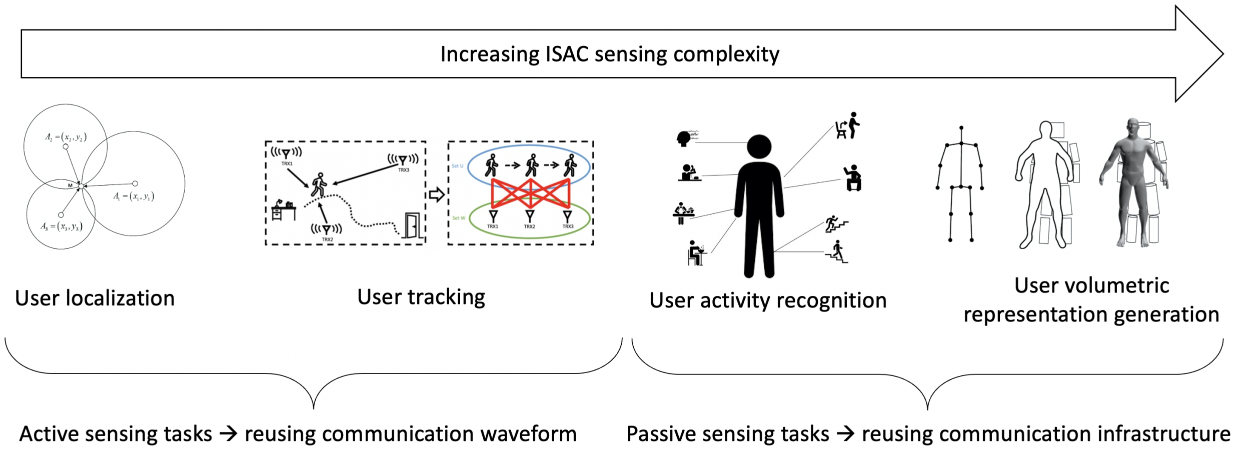

Figure 3: Example ISAC sensing tasks ordered by implementation complexity

without the necessity for channel state information (CSI) [5]. Furthermore, Zhou *et al.* studied a latency minimization problem for a multi-user secure IRS-aided VR delivery network with imperfect Channel State Information (CSI) [51].

Nonetheless, these studies have not explored the potential synergies of melding IRS with mmWave communication and sensing in a full-immersive multi-user VR scenario. Moreover, the incorporation of IRSs in multi-user VR streaming systems, especially with optimal resource allocation, remains uncharted territory. Within IRS-enhanced VR streaming systems, the meticulous optimization of IRS phase shifts, placement, radiation patterns, and beamforming vectors stands vital to realizing high data rates. To the best of our knowledge, none of the research works have optimized the design of an IRS-assisted indoor VR network, where the IRS is considered to be deployed in a confined 3D space as a function of VR users' trajectory.

2.3 Real-Time Sensing for Enhanced Experiences

MmWave Joint Communication and Sensing (JCAS) is a new paradigm gaining traction in the context of Sixth Generation (6G). The idea is for mmWave networks to support sensing in addition to supporting more traditional communication requirements. Integrated sensing can be performed with different aims, depending on the application scenario. For example, localization is one typical example of sensing in mmWave JCAS systems [20], which finds applications in e.g., vehicular networking scenarios [35]. More advanced applications can be found in the considered VR-specific scenario. Some examples include estimation of human pose or activities using mmWave signals [6], while more advanced ones envision full-body 3D representation capturing [40]. This advanced functionality is then envisioned to be used as a primer for generating interactive VEs with realistic 3D avatars prudently tracking users' movements. It has been established in [47] that, in high-frequency communication, there is a direct link between sensing accuracy and SNR. When deploying an JCAS network, a single waveform transmits data and performs radar detection simultaneously. The waveform must be capable of accommodating radar detection requirements such as estimation accuracy. Range, speed and communication requirements such as reliability, throughput, and latency necessitate a minimum SNR to function correctly, which is critical for reliable and accurate signal detection and interpretation. Hence, optimizing the sensing accuracy requires maintaining stable and high SNR across the deployment environment, which is addressed through the utilization of IRS.

While IRS was designed primarily for communication, the technology may bring significant benefits regarding performance, power consumption, and cost for localization and mapping, which is a promising function. As such, IRS-assisted JCAS systems have been extensively researched in various scenarios. The work [17] investigates the joint design of transmit beamforming at the AP and reflection coefficients at the IRS to maximize the SNR of radar detection while meeting the communication need. The authors in [34] propose a two-dimensional hierarchical code book that simultaneously services the User Equipment (UE) and locates the target using the IRS for location and communication. In [25], the authors propose a new simultaneous (beam) training and sensing (STAS) protocol that utilizes downlink IRS beam scanning for concurrent training and sensing to achieve efficient IRS-aided mmWave JCAS. And finally, [14] proposes an JCAS system by introducing an IRS architecture to the communication system where location sensing and data transmission can be conducted simultaneously, occupying the same spectrum and time resources.

In general, channel parameters such as Time of Arrival (ToA)/Time Difference of Arrival (TDoA), Angle of Arrival (AoA), and Received Signal Strength (RSS) can be used for enabling the sensing tasks outlined in Figure 3. Taking user localization as an example, RSS-based localization has poor location accuracy, which is influenced by network topology and propagation environment factors such as path loss exponent and shadowing effects. Although ToA/TDoA-based and AoA-based localization can achieve high location accuracy, they rely heavily on the LoS link, which can be disrupted, particularly in the mmWave case. As a result of its ability to establish a strong LoS path between the AP and the UE, the IRS has been proposed to overcome the blockage problem and improve location accuracy in the wireless communication system [14]. These properties, combined with their close relation to the environment's geometry and ability to be embedded in soft materials, as mentioned in [19], enable IRS to function as a "barrier" that defines the boundaries of the deployment environment and makes them desirable for mapping and localization purposes.

3 Overcoming Communication and Sensing Challenges

3.1 Considered Scenario

We consider a scenario as depicted in Figure 4. Specifically, we consider an environment in which the users are immersed in their VEs. The environment is constrained in its physical size as to provide a safe space for the users to immerse in their experiences. As such, the only potential collision perils for the users are other users and environmental boundaries. RDW is employed for directing the users primarily in a way that does not break their immersion, as discussed in Section 2. The users are immersed in VEs that are potentially unbound and interactive in the way that the action of one user affects the experience of the other, potentially collocated users. The perception of unbounded experiences are supported through RDW by introducing imperceivable rotational, translational, and curvature gains, as discussed previously.

In such a scenario, the goal is to provide the users with the consistently high throughput throughout their VEs. As such, the communication throughput between the AP and the users' HMD should be maximized, while simultaneously providing homogeneous coverage or minimizing the spatial variability of the throughput. This is of interest as it allows for downlink transmission of the video content toward the users' HMDs in a way that minimizes the jitter and allows for continuous delivery of same-quality video frames. The fact that the users' VEs might be interactive poses an additional system requirement. Specifically, there is a need for capturing the actions of the users, as well as delivering the captured content to other users, where both actions should be carried out within the motion-to-photon latency for immersion maximization and avoiding the motion sickness.

To support the outlined scenario's requirements, we envision the utilization of high-frequency wireless networks operating in mmWave frequencies (i.e., 30-300 GHz). This is because the delivery of VR content in real time, as well as real time sensing and distribution of users' actions across other users, requires significant communication bandwidth not present in traditional sub-6 GHz frequencies. In addition, large communication bandwidth available at such frequencies represents a primer for accurate network-supported sensing of users' actions, e.g., in the form of digital capturing of users full 3D poses.

Due to all these needs for our scenario, we have used IEEE 802.11ad networks. The IEEE 802.11ad standard operates at mmWave frequencies, which makes directional communication a feature to allow high speeds over short distances. This is achieved through advanced beamforming techniques, in which the AP and UEs can focus their transmissions in specific directions, improving signal strength and reliability. However, this directional nature of communication can create challenges in achieving uniform coverage within a given area [28]. The quality in the formation of beams varies with the number of antennas; as the number of antennas increases, the width of the beam is reduced, making the array more directional, thus improving beamforming. At the same time, as the number of antennas decreases, the beamforming declines [36]. When the number of antenna elements in a AP is limited, achieving uniform coverage over the entire area becomes difficult. This limitation can result in areas of weaker signal strength or coverage gaps, which can be particularly problematic for applications such as VR.

To counter these challenge, we introduce IRSs to the considered full-immersive multiuser VR environments. Given that such environments will have to be safe spaces without collision hazards for the users apart from the environmental boundaries and other users [4], we consider it as a natural possibility to utilize IRSs in the surrounding walls to support the communication and sensing challenges stemming from the scenario. IRSs consist of large arrays of passive reflecting elements on a reconfigurable planar surface. These elements can independently modify the phase of an incoming signal before reflecting it towards its intended receiver. The integration of IRS can be a boon for users experiencing significant path loss, as the IRS creates additional propagation pathways – namely, reflected channels. Moreover, these IRSs offer added degrees of freedom through the phase shifts of the reflective elements, which can be harnessed to minimize interference [15]. It is also worth noting that IRSs are envisioned to be manufactures as passive, cheap, and flexible entities adaptable for indoor VR streaming setups, as they could be used as 'soft' environmental boundaries [19].

For the full-immersive VR scenario in Figure 4, we study a novel radio resource allocation optimization in an IRS-assisted mmWave network, where a multi-antenna AP transmits information symbols to a set of single-antenna HMDs. In particular, a resource allocation algorithm is

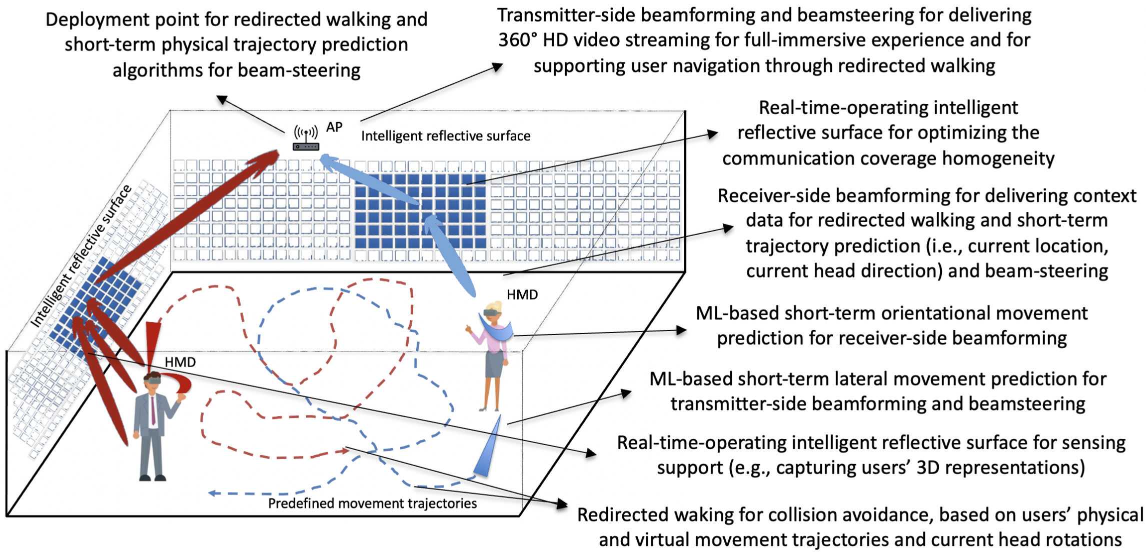

Figure 4: Considered full-immersive IRS-assisted mmWave scenario.

designed to maximize the system's sum data-rate subject to peak transmit power feasibility and QoS constraints. The formulated problem is non-convex due to the high coupling of optimization variables. To tackle this, we employ AO algorithm, segmenting the main optimization problem into four distinct sub-problems, in which each sub-problem is optimally solved.

3.2 Location-based IRS Resource Allocation for Communication and Active Sensing

As depicted in Fig. 1, we study a wireless communication system in which IRS are used to redirect data to a set of UEs. The set of all UEs is represented as $\mathcal{K} = \{1, ..., K\}$ and the set of IRS elements is denoted by $\mathcal{M} = \{1, ..., M\}$. In many real-world applications, utilizing IRS for wireless communication proves beneficial. For instance, in applications that can tolerate delays like periodic sensing data collection, using IRS to sequentially communicate with UEs can be an economical choice. Our goal is to fine tune the IRSs' position to achieve maximum SNR over a fixed time span $T > 0$. As explained in Section 2, it is critical to maintain a high SNR to provide extensive and reliable coverage to deliver stronger signals, reduced dead zones and improved comprehensive data collection to enhance communication and sensing. The time duration T is partitioned into N uniformly spaced time intervals, given by $T = N\xi_t$. Specifically, ξ_t denotes the length of each individual time slot, and N is defined as the set of all these time slots, represented by $\mathcal{N} = \{1, ..., N\}$.

In this context, we are adopting a 3D Cartesian coordinate system with the AP situated at a fixed location $\boldsymbol{a} = [a_x, a_y, a_z]^T \in \mathbb{R}^{3\times1}$. On the other hand, the UEs are placed in a ground location, and their trajectory follows the path $\boldsymbol{u}[n,k] = [u_x[n,k], u_y[n,k], u_z[n,k]]^T \in \mathbb{R}^{3\times1}$.

The placement of the IRSs', when projected onto the horizontal plane, is represented by $\boldsymbol{s}[n] = [s_x[n], s_y[n], s_z[n]]^T \in \mathbb{R}^{3\times1}$. Furthermore, we confine the area of interest to four half-have spaces H_1 to H_4 where the IRSs' could potentially be placed. The half spaces H_1 to H_4 can be defined as follows:

$$H_1 : y_{min} < s_y[n] < y_{max}, z_{min} < s_z[n] < z_{max}, s_x[n] = x_{mix}, \tag{1}$$
$$H_2 : y_{min} < s_y[n] < y_{max}, z_{min} < s_z[n] < z_{max}, s_x[n] = x_{max}, \tag{2}$$
$$H_3 : x_{min} < s_x[n] < x_{max}, z_{min} < s_z[n] < z_{max}, s_y[n] = y_{min}, \tag{3}$$
$$H_4 : x_{min} < s_x[n] < x_{max}, z_{min} < s_z[n] < z_{max}, s_y[n] = y_{max} \tag{4}$$

These regions make sure that IRSs' are positioned in one of the corner walls of the room. In this configuration, the distance between the IRS and the UE, as well as between the IRS and the AP over time, has a direct influence on the channel quality. Consequently, determining the optimal positioning of the IRS becomes crucial.

To clarify our discussion, we operate under the assumption that the communication link between the IRS and the UEs is largely governed by the LoS channel. In the context of our setup, it is important to highlight that the IRS-UE channel is more inclined to maintain a prominent LoS link than AP-UE channels. For this explanation, we also assume that the AP-UE channel is entirely obstructed by other UE that block the LoS between the AP and the UE. Exploring Non-Line-of-Sight (NLoS) and multi-path fading channels will be reserved for our subsequent studies. Additionally, any Doppler effect caused by the UE's mobility is presumed to be fully compensated for.

To expedite the utilization of an IRS-aided communication, we also take into account the radiation pattern of the IRS, as explored in [41], namely:

$$F(\psi,\varphi)=\begin{cases}\cos^3(\psi), & \psi\in[0,\pi/2],\varphi\in[0,2\pi],\\ 0, & \psi\in(\pi/2,\pi],\varphi\in[0,2\pi],\end{cases} \tag{5}$$

where ψ and φ represent the elevation and azimuth angles, respectively, from the IRS to the AP/UE link. It is worth pointing out that the radiation pattern of the IRS remains consistent across various azimuth angles. To streamline our discussion, we exclude the argument φ from the function $F(\psi,\varphi)$ in (23) in subsequent equations, using $F(\psi)$ in place of $F(\psi,\varphi)$. Given these conditions, the dynamic channel between AP and IRS, and between IRS and the k-th UE adheres to the free-space path loss model, which can be detailed as:

$$\tilde{\mathbf{h}}=\mathbf{h}\sqrt{\beta_0 F(\psi_0)}, \tag{6}$$

$$\tilde{\mathbf{g}}_k=\mathbf{g}_k\sqrt{\beta_k F(\psi_k)},\forall k\in\mathcal{K}, \tag{7}$$

where β_0 and β_k symbolize the path loss, while $\mathbf{h}\in\mathbb{C}^{M\times 1}$ and $\mathbf{g}_k\in\mathbb{C}^{M\times 1}$ stand for the small-scale fading of the links between AP and IRS and between IRS and the k-th UE, respectively. Notably, the small-scale fading remains static throughout each coherence interval. In contrast, the path loss undergoes changes but at a much slower rate. This perspective is justifiable when considering that the distances between the users, the AP, and the IRS are significantly larger than the separations between the IRS elements [7, 48]. In light of this, β_0 and β_k can be delineated as:

$$\beta_{k'}=c_0\|\mathbf{d}_{k'}\|^{-\alpha_{k'}},\ k'\in\mathcal{K}\cup\{0\}, \tag{8}$$

where c_0 is the reference path loss at a distance of 1 meter. α_0 and $\alpha_k,\forall k\in\mathcal{K}$ are the path loss exponents of links between AP and IRS and the link between IRS and UE k, respectively [26]. Moreover, the distance vectors from the IRS to the AP and k-th UE are respectively given by:

$$\mathbf{d}_0=\boldsymbol{s}[n]-\boldsymbol{a}[s_x[n]-a_x,s_y[n]-a_y,s_z[n]-a_z]^T,\forall n\in\mathcal{N}, \tag{9}$$

$$\begin{aligned}\mathbf{d}_k=\boldsymbol{s}[n]-\boldsymbol{u}[n,k]=[&s_x[n]-u_x[n,k],s_y[n]-u_y[n,k],\\ &s_z[n]-u_z[n,k]]^T,\\ &\forall n\in\mathcal{N},\forall k\in\mathcal{K}.\end{aligned} \tag{10}$$

Finally, the received signal of k-th UE can be mathematically expressed as:

$$y_k=\sqrt{P_{\text{AP}}}\tilde{\mathbf{g}}_k^H\boldsymbol{\Theta}\tilde{\mathbf{h}}+n_k,\forall k\in\mathcal{K}, \tag{11}$$

where P_{AP} is the access point transmit power and n_k is the additive white Gaussian noise (AWGN) at k-th UE, which follows a complex normal distribution with mean 0 and variance σ_k^2. The IRS phase shift matrix is represented by $\boldsymbol{\Theta}$ and is defined as $\boldsymbol{\Theta}\equiv\text{diag}(\theta_1,\theta_2,\ldots,\theta_M)$. Here, $\theta_m\in\mathbb{C}$ characterizes the reflection coefficient of the m-th IRS element. Specifically, $\theta_m\equiv\varrho_m e^{j\vartheta_m}$, where ϱ_m lies within $[0,1]$, capturing the reflection amplitude, and ϑ_m spanning $[0,2\pi]$ depicts the phase shift of the m-th IRS element. Notably, the 'j' in the exponent represents the imaginary unit. Ultimately, by assuming there is no multi-user interference, we represent the SNR at k-th UE as follows:

$$\gamma_k(P_{\mathrm{AP}}, \boldsymbol{\Psi}, \boldsymbol{\beta}, \boldsymbol{\Theta}) = \frac{P_{\mathrm{AP}}\beta_0 F(\psi_0)\beta_k F(\psi_k)\left|\mathbf{g}_k^H \boldsymbol{\Theta}\mathbf{h}\right|^2}{\sigma_k^2}, \forall k \in \mathcal{K}, \tag{12}$$

where $\boldsymbol{\Psi}$ and $\boldsymbol{\beta}$ are the collection of ψ's and β's according to $\boldsymbol{\Psi} \triangleq [\psi_0, ..., \psi_K]$ and $\boldsymbol{\beta} \triangleq [\beta_0, ..., \beta_K]$, refer to the IRS location decision variables, $\boldsymbol{s}[n]$. Given the SNR expression as articulated above, in equation (12), the Spectral Efficiency (SE) for k-th UE, measured in [bit/s/Hz], can be expressed as:

$$R(P_{\mathrm{AP}}, \boldsymbol{\Psi}, \boldsymbol{\beta}, \boldsymbol{\Theta}) = log_2(1 + \gamma_k(P_{\mathrm{AP}}, \boldsymbol{\Psi}, \boldsymbol{\beta}, \boldsymbol{\Theta})), \forall k \in \mathcal{K}, \tag{13}$$

consequently, the sum data-rate for all UEs can be written as:

$$R_{\mathtt{tot}}(P_{\mathrm{AP}}, \boldsymbol{\Psi}, \boldsymbol{\beta}, \boldsymbol{\Theta}) = B \sum_{\forall k \in \mathcal{K}} R(P_{\mathrm{AP}}, \boldsymbol{\Psi}, \boldsymbol{\beta}, \boldsymbol{\Theta}), \tag{14}$$

where B represents the bandwidth of the network. In the context of our study, it is also of high importance to enhance the total data-rate. This can be achieved by fine-tuning parameters such as transmit power control, optimal placement of IRS, and their corresponding phase shifts. With this objective in mind, the optimization problem can be formulated as:

$$\mathrm{P}_1 : \max_{P_{\mathrm{AP}}, \boldsymbol{\Psi}, \boldsymbol{\beta}, \boldsymbol{\Theta}} R_{\mathtt{tot}}(P_{\mathrm{AP}}, \boldsymbol{\Psi}, \boldsymbol{\beta}, \boldsymbol{\Theta}), \tag{15a}$$

$$\text{s.t. } P_{\mathrm{AP}} \le P_{\mathtt{AP}}^{\max}, \tag{15b}$$

$$|\theta_m| \le 1, \ \forall m \in \mathcal{M}, \tag{15c}$$

$$(22). \tag{15d}$$

Constraint (15b) ensures that the transmission power remains within the upper limits set for the AP. Constraint (15c) specifies the bounds within which the reflection coefficient for every IRS element must operate. Constraint (22) ensure IRSs' are positioned in one of the corner walls of the room. Given the presence of a non-concave objective function and the non-convex nature of constraint (15c), the optimization problem laid out in (15) is distinctly nonconvex. This inherent complexity makes it challenging to derive a straightforward solution for the problem. As a result, AO methods or approximations might be needed to effectively address non-convexity.

3.2.1 AP Transmit Power Control

We first fix $\boldsymbol{\Psi}$, $\boldsymbol{\beta}$, and $\boldsymbol{\Theta}$, and consider the optimization of P_{AP}. Thus, the corresponding optimization problem of AP transmit power control [24] with a transformed objective function can then be formulated as follows:

$$\mathrm{P}_2 : \max_{P_{\mathrm{AP}}} \sum_{\forall k \in \mathcal{K}} \frac{P_{\mathrm{AP}}\beta_0 F(\psi_0)\beta_k F(\psi_k)\left|\mathbf{g}_k^H \boldsymbol{\Theta}\mathbf{h}\right|^2}{\sigma_k^2}, \tag{16a}$$

$$\text{s.t. } P_{\mathrm{AP}} \le P_{\mathtt{AP}}^{\max}. \tag{16b}$$

One can readily prove that the optimization problem (16) is affine and convex. Thus, we can exploit the properties of convex optimization to derive solutions. To do so, one approach is to differentiate the objective function concerning P_{AP}, the AP transmit power. By setting this first-order derivative to zero and taking into account the constraint that dictates the maximum transmit power, we can derive the optimal solution for the problem described in (16). This solution can be represented as $P_{\mathrm{AP}} = \max\left\{0, P_{\mathtt{AP}}^{\max}\right\}$.

3.2.2 IRS Optimal Placement

In this subsection, we formulate the subproblem wherein the IRSs' placement are optimized with a fixed IRS phase shift and radiation pattern, i.e., $\boldsymbol{\Psi}$ and $\boldsymbol{\Theta}$ are known. Therefore, the optimization problem for the IRSs' position can be written as follows:

$$\mathrm{P}_3 : \max_{\boldsymbol{s}[n]} \sum_{\forall k \in \mathcal{K}} \frac{c_0^2 F(\psi_0) F(\psi_k) \left|\mathbf{g}_k^H \boldsymbol{\Theta} \mathbf{h}\right|^2}{\sigma_k^2 \|\boldsymbol{s}[n]-\boldsymbol{a}\|^{\alpha_0} \|\boldsymbol{s}[n]-\boldsymbol{u}[n,k]\|^{\alpha_k}}, \tag{17a}$$

$$\text{s.t. } (22), \tag{17b}$$

where $\boldsymbol{\beta}$'s are replaced by the IRSs' location decision variables, $\boldsymbol{s}[n]$. It can be seen optimization problem (17). Thus, an optimal solution that gives can be found. By setting the first-order derivative of the objective function with respect to $\boldsymbol{s}[n]$ to zero and considering the maximum SNR, we obtain the following two qualities:

$$\begin{aligned} &\frac{(a_x - s_x[n])}{(a_x - s_x[n])^2 + (a_y - s_y[n])^2 + (a_z - s_z[n])^2} \\ &= \frac{(s_x[n] - u_y[n,k])}{(s_x[n] - u_y[n,k])^2 + (s_y[n] - u_y[n,k])^2 + (s_z[n] - u_z[n,k])^2} \end{aligned} \tag{18}$$

$$\begin{aligned} &\frac{(a_y - s_y[n])}{(a_x - s_x[n])^2 + (a_y - s_y[n])^2 + (a_z - s_z[n])^2} \\ &= \frac{(s_y[n] - u_y[n,k])}{(s_x[n] - u_y[n,k])^2 + (s_y[n] - u_y[n,k])^2 + (s_z[n] - u_z[n,k])^2} \end{aligned} \tag{19}$$

$$\begin{aligned} &\frac{(a_z - s_z[n])}{(a_x - s_x[n])^2 + (a_y - s_y[n])^2 + (a_z - s_z[n])^2} \\ &= \frac{(s_z[n] - u_z[n,k])}{(s_x[n] - u_y[n,k])^2 + (s_y[n] - u_y[n,k])^2 + (s_z[n] - u_z[n,k])^2} \end{aligned} \tag{20}$$

where it is assumed $\alpha_k = 2$ [23] in order to achieve closed-from solutions. Given the aforementioned inequalities, an iterative approach is employed to determine the optimal IRSs' position. Starting with predetermined or initial values for $s_x[n]$, $s_y[n]$, and $s_z[n]$, the optimal x-coordinate, y-coordinate and z-coordinate of the IRS are computed using the equation referenced by $(34)-(20)$ iteratively and following the constraint (22). This iterative refinement converges to optimize the IRS's placement in the 3D plane based on the system's performance metric and constraints. The iterative algorithm is given in Algorithm 1.

3.2.3 Passive Beamforming and Radiation Pattern Optimization at the IRS

We now consider the subproblem of jointly optimizing $\boldsymbol{\Psi}$ and $\boldsymbol{\Theta}$ with fixed P_{AP} and $\boldsymbol{\beta}$, which can be given by:

$$\mathrm{P}_4 : \max_{\boldsymbol{\Psi}, \boldsymbol{\Theta}} R_{\mathtt{tot}}(\boldsymbol{\Psi}, \boldsymbol{\Theta}), \tag{21a}$$

$$\text{s.t. } |\theta_m| \leq 1, \ \forall m \in \mathcal{M}. \tag{21b}$$

Unlike the preceding two subproblems that have closed-form solutions, obtaining a closed-form solution for $\boldsymbol{\Psi}$ and $\boldsymbol{\Theta}$ is challenging due primarily to the constraints associated with the IRS unit modulus. Fortunately, we could utilize successive convex approximation methods to transform the rank unit modulo constraint into linear matrix inequalities per iteration based on [15]. The Final iterative-based AO algorithm is provided in Algorithm 2.

3.3 Location-based IRS Resource Allocation for Advanced Sensing

In many real-world applications, the utilization of IRS for wireless communication proves to be advantageous. For instance, employing IRS sequentially communicate with UE can be a cost-effective choice in scenarios where delays cannot be tolerated, such as periodic sensing data collection, as is the case in high data-rate Virtual Reality (VR) networks. As illustrated in Fig. 4, we investigate a wireless communication system in which IRSs are employed to redirect data to a set of UEs. The

Algorithm 1 IRS Optimal Placement algorithm

Input: Initial parameters $s_x[n], s_y[n], s_z[n]$, maximum iterations I (with i as the iteration index) and precision P

Output: Optimal parameters $s_x[n]^*, s_y[n]^*, s_z[n]^*$

repeat
  $p_{s_x[n]} = s_x[n]$
  $p_{s_y[n]} = s_y[n]$
  $p_{s_z[n]} = s_z[n]$
  Compute gradient vector for 18 $\nabla J(s_x[n])$
  Compute gradient vector for 19 $\nabla J(s_y[n])$
  Compute gradient vector for 20 $\nabla J(s_z[n])$
  Update parameters: $s_x[n] \leftarrow s_x[n] + \alpha \cdot \nabla J(s_x[n])$
  Update parameters: $s_y[n] \leftarrow s_y[n] + \alpha \cdot \nabla J(s_y[n])$
  Update parameters: $s_z[n] \leftarrow s_z[n] + \alpha \cdot \nabla J(s_z[n])$
  $p = ||s_x[n] - p_{s_x[n]}|| + ||s_y[n] - p_{s_y[n]}|| + ||s_z[n] - p_{s_z[n]}||$
  $i \leftarrow i + 1$
until $p < P$ and $i < I$
return $s_x[n]^* = s_x[n], s_y[n]^* = s_y[n], s_z[n]^* = s_z[n]$

Algorithm 2 Iterative AO Algorithm

Input: Set iteration number $e = 0$, maximum number of iterations $E_{\max}$, and and initialize the coordinates $P_{\text{AP}} = P_{\text{AP}}^0$, $\mathbf{\Psi}_e = \mathbf{\Psi}_e^0$, $\boldsymbol{\beta}_e = \boldsymbol{\beta}_i^0$, $\mathbf{\Theta}_e = \mathbf{\Theta}_e^0$.

repeat
  Solve problem (16) for given $\{\mathbf{\Psi}_i^{e-1}, \boldsymbol{\beta}_i^{e-1}, \mathbf{\Theta}_i^{e-1}\}$ and obtain the optimal P_{AP}^e.
  Solve problem (17) for given $\{P_{\text{AP}}^{e-1}, \mathbf{\Psi}_i^{e-1}, \mathbf{\Theta}_i^{e-1}\}$ and obtain the optimal $\boldsymbol{\beta}_i^e$.
  Solve problem (21) for given $\{P_{\text{AP}}^{e-1}, \boldsymbol{\beta}_i^{e-1}\}$ and obtain the sub-optimal $\{\mathbf{\Psi}_i^e, \mathbf{\Theta}_i^e\}$.
until e = $E_{\max}$
return $\{P_{\text{AP}}^*, \mathbf{\Psi}_i^*, \boldsymbol{\beta}_i^*, \mathbf{\Theta}_i^*\}$=$\{P_{\text{AP}}^e, \mathbf{\Psi}_i^e, \boldsymbol{\beta}_i^e, \mathbf{\Theta}_i^e\}$

collection of all UEs is denoted as $\mathcal{K} = 1, ..., K$, while the set of IRSs is represented as $\mathcal{I} = 1, ..., I$, with each element of an IRS being denoted by $\mathcal{M} = 1, ..., M$. Our objective is to optimize the position of the IRSs to maximize the Signal-to-Noise Ratio (SNR) over a fixed time duration $T > 0$. Sustaining a high SNR is of paramount importance to ensure extensive and dependable coverage, leading to stronger signals, minimized dead zones, and enhanced comprehensive data collection, ultimately improving communication and sensing capabilities. The time duration T is divided into N evenly spaced time intervals, defined as $T = N\xi_t$. More precisely, ξ_t signifies the duration of each individual time slot, and N represents the set of all these time slots, denoted as $\mathcal{N} = 1, ..., N$.

In this context, we utilize a 3D Cartesian coordinate system to track the positions of the AP, UEs, and IRSs. The AP is fixed at coordinates $\boldsymbol{a} = [a_x, a_y, a_z]^T \in \mathbb{R}^{3\times 1}$. On the other hand, the UEs are randomly scattered in a vertical plane, and their predefined trajectory follows the path $\boldsymbol{u}[n,k] = [u_x[n,k], u_y[n,k], u_z[n,k]]^T \in \mathbb{R}^{3\times 1}$. The placement of the IRSs' is pivotal for signal redirection. When projected onto the vertical plane (e.g., on each wall of a room or office enforcement), the central location of i-th IRS is represented by $\boldsymbol{s}^i[n] = [s_x^i[n], s_y^i[n], s_z^i[n]]^T \in \mathbb{R}^{3\times 1}$.

Furthermore, we confine the area of interest to $\mathcal{I}$ half-have spaces $\mathcal{D}_\infty = \{\mathcal{D}_1, \ldots, \mathcal{D}_I\}$ where each IRSs' could potentially be placed[5]. Within the first half-space, the first IRS can be strategically positioned, and as such, we define $\mathcal{D}_1$ as:

[5] We strategically place each IRS central position in any of these half-space regions to optimize signal quality, minimize interference, and enhance overall wireless communication system efficiency. This is done so long as no two IRS are placed in one half-space; that is, each IRS must be positioned in a different half-space.

$$
\begin{aligned}
x^i_{min} <& s^i_x[n] < x^i_{max},\\
y^i_{min} <& s^i_y[n] < y^i_{max},\\
z^i_{min} <& s^i_z[n] < z^i_{max},\ \forall n \in \mathcal{N}, \forall i \in \mathcal{I},
\end{aligned} \tag{22}
$$

The domain in (22) defines the first region, i.e., $\mathcal{D}_1$, where the first IRS needs to be centrally positioned. Likewise, we can establish $\mathcal{D}_\infty/\mathcal{D}_1 = \{\mathcal{D}_2, \ldots, \mathcal{D}_I\}$ to represent the regions within which the remaining IRSs are positioned. These regions make sure that IRSs' are positioned in one of the corner walls of the room as depicted in Fig. 4.

In this configuration, the distance between the IRS and the UE, as well as between the IRS and the AP, evolves over time and significantly impacts the quality of the communication channel. Therefore, determining the optimal placement of the IRS is of utmost importance. To provide clarity to our discussion, we make the assumption that the communication link between the IRS and the UE is predominantly governed by the LoS channel. It is noteworthy that, within our setup, the IRS-UE channel is more likely to maintain a strong LoS link compared to the AP-UE channels. We make this assumption while considering that the AP-UE channel is entirely obstructed by other UEs, which block the LoS between the AP and the UE. We reserve the exploration of NLoS and multi-path fading channels for our future studies. Additionally, we presume that any Doppler effect induced by UE mobility is fully compensated for in our analysis. To expedite the utilization of an IRS-aided communication, we also take into account the radiation pattern of the IRS, as explored in [41], namely:

$$
F(\psi_{i,k}, \varphi_i) = \begin{cases} \cos^3(\psi_{i,k}), & \psi_{i,k} \in [0, \pi/2], \varphi_i \in [0, 2\pi], \\ 0, & \psi_{i,k} \in (\pi/2, \pi], \varphi_i \in [0, 2\pi], \end{cases} \tag{23}
$$

where $\psi_{i,k}$ and φ_i represent the elevation and azimuth angles, respectively, from each IRS to the AP/UE link. It is important to note that the radiation pattern of the IRS remains consistent across various azimuth angles. To simplify our discussion, we omit the argument φ_i from the function $F(\psi_{i,k}, \varphi_i)$ in (23) in subsequent equations, using $F(\psi_{i,k})$ in place of $F(\psi_{i,k}, \varphi_i)$. Under these conditions, the dynamic channel between the AP and the IRS, as well as between the IRS and the k-th UE, follows the free-space path loss model, which can be described as:

$$
\tilde{\mathbf{h}_i} = \mathbf{h}_i \sqrt{\beta_{i,0} F(\psi_{i,0})}, \tag{24}
$$

$$
\tilde{\mathbf{g}}_{i,k} = \mathbf{g}_{i,k} \sqrt{\beta_{i,k} F(\psi_{i,k})}, \forall k \in \mathcal{K}, \tag{25}
$$

where $\beta_{i,0}$ and $\beta_{i,k}$ serve to quantify path loss, representing the reduction in signal strength as it traverses the wireless medium. In contrast, the vectors $\mathbf{h}_i \in \mathbb{C}^{M\times 1}$ and $\mathbf{g}_{i,k} \in \mathbb{C}^{M\times 1}$ describe small-scale fading, accounting for the rapid signal fluctuations attributed to phenomena like multipath propagation and signal scattering. Notably, these small-scale fading characteristics exhibit relative stability throughout each coherence interval, allowing us to treat them as quasi-static. Meanwhile, path loss, influenced by distance and environmental obstructions, undergoes variations, albeit at a much slower pace. This perspective is rooted in the substantial difference in scales between the distances separating users, the AP, and the IRS and the distances between individual IRS elements, where variations occur much more swiftly and are, therefore, considered negligible in comparison, aligning with existing wireless communication literature [7, 2]. In light of this, the path loss components can be represented as:

$$
\beta_{i,k'} = c_0 \|\mathbf{d}_{i,k'}[n]\|^{-\alpha_{i,k'}}, \forall k' \in \mathcal{K} \cup \{0\}, \forall i \in \mathcal{I}, \forall n \in \mathcal{N}, \tag{26}
$$

where c_0 is the reference path loss at a distance of 1 meter.

$\alpha_{i,0}$ and $\alpha_{i,k}, \forall k \in \mathcal{K}$ are the path loss exponents of links between AP and IRS and the link between IRS and UE k, respectively [13]. Moreover, the distance vectors from the IRS to the AP and k-th UE are respectively given by:

$$\begin{aligned}\mathbf{d}_{i,0}[n] =& \boldsymbol{s}^i[n] - \boldsymbol{a}[s_x^i[n] - a_x, s_y^i[n] - a_y, s_z^i[n] - a_z]^T,\\ & \forall i \in \mathcal{I},\ \forall n \in \mathcal{N},\end{aligned} \tag{27}$$

$$\begin{aligned}\mathbf{d}_{i,k}[n] =& \boldsymbol{s}^i[n] - \boldsymbol{u}[n,k] = [s_x^i[n] - u_x[n,k], s_y^i[n] - u_y[n,k],\\ & s_z^i[n] - u_z[n,k]]^T,\\ & \forall k \in \mathcal{K},\ \forall i \in \mathcal{I},\ \forall n \in \mathcal{N}.\end{aligned} \tag{28}$$

To sum it up, the mathematical representation for the received signal at the k-th UE is as follows:

$$y_k = \sum_{i\in\mathcal{I}} \sqrt{P_{\mathrm{AP}}}\tilde{\mathbf{g}}_{i,k}^H \mathbf{\Theta}_i \tilde{\mathbf{h}}_i + n_k, \forall k \in \mathcal{K}. \tag{29}$$

where P_{AP} is the transmit power of the AP, and n_k corresponds to the additive white Gaussian noise (AWGN) observed at the k-th UE. The noise follows a complex normal distribution characterized by a mean of zero and a variance of σ_k^2. The i-th IRS phase shift matrix is represented by $\mathbf{\Theta}_i$ and is defined as $\mathbf{\Theta}_i \equiv \mathrm{diag}\ (\theta_{1,m}, \theta_{2,m}, \ldots, \theta_{i,M})$. Here, $\theta_{i,m} \in \mathbb{C}$ characterizes the reflection coefficient associated with the m-th element of the i-th IRS. Specifically, $\theta_{i,m} \equiv \varrho_{i,m} e^{j\vartheta_{i,m}}$, where $\varrho_{i,m}$ lies within $[0,1]$, capturing the reflection amplitude, and $\vartheta_{i,m}$ spanning $[0,2\pi]$ depicts the phase shift of the m-th element of the i-th IRS. It is worth noting that the exponent 'j' in the equation represents the imaginary unit. In the absence of multi-user interference, we can express the SNR at the k-th UE as follows:

$$\begin{aligned}\gamma_{i,k}(P_{\mathrm{AP}}, \mathbf{\Psi}_i, \boldsymbol{\beta}_i, \mathbf{\Theta}_i) = \frac{P_{\mathrm{AP}}\beta_{i,0}F(\psi_{i,0})\beta_{i,k}F(\psi_{i,k})\left|\mathbf{g}_{i,k}^H\mathbf{\Theta}_i\mathbf{h}_i\right|^2}{\sigma_k^2},\\ \forall k \in \mathcal{K}, \forall i \in \mathcal{I},\end{aligned} \tag{30}$$

where $\mathbf{\Psi}_i$ and $\boldsymbol{\beta}_i$ encompass the sets of $\psi_{i,k}$'s and $\beta_{i,k}$'s, organized respectively as follows: $\mathbf{\Psi}_i \triangleq [\psi_{i,0}, ..., \psi_{i,K}]$ and $\boldsymbol{\beta}_i \triangleq [\beta i, 0, ..., \beta_{i,K}]$. These variables are instrumental in representing each IRS location decision variable in terms of $\boldsymbol{\beta}_i$. Given the SNR expression as articulated above, the optimization problem can be formulated as:

$$\mathrm{P}_5: \max_{P_{\mathrm{AP}}, \mathbf{\Psi}_i, \boldsymbol{\beta}_i, \mathbf{\Theta}_i} \gamma_{i,k}(P_{\mathrm{AP}}, \mathbf{\Psi}_i, \boldsymbol{\beta}_i, \mathbf{\Theta}_i), \tag{31a}$$

$$\text{s.t. } P_{\mathrm{AP}} \leq P_{\mathtt{AP}}^{\max}, \tag{31b}$$

$$|\theta_{i,m}| \leq 1,\ \forall m \in \mathcal{M}, \forall\ i \in \mathcal{I}, \tag{31c}$$

$$\boldsymbol{s}^i[n] \in \mathcal{D}_i, \forall\ i \in\ \mathcal{I},\ \forall n \in \mathcal{N}. \tag{31d}$$

Constraint (31b) guarantees that the transmission power of the AP remains within the specified upper limits. Constraint (31c) defines the operational boundaries for the reflection coefficients of each IRS element. Constraint (31d) enforces the placement of IRSs on one of the corner walls of the room. Due to the presence of a non-concave objective function and the non-convex nature of constraint (31c), the optimization problem outlined in (31) is inherently nonconvex. This complexity poses a challenge in finding an optimal solution to the problem. Consequently, addressing non-convexity may require the use of optimization techniques or approximations, such as Alternating Optimization (AO) methods, to effectively tackle the problem.

3.3.1 AP Transmit Power Control

To start, we hold $\mathbf{\Psi}_i$, $\boldsymbol{\beta}_i$, and $\mathbf{\Theta}_i$ fixed and concentrate on optimizing P_{AP}. Consequently, we formulate the optimization problem for AP transmit power control [24, 43] as follows:

$$\mathrm{P}_6: \max_{P_{\mathrm{AP}}} \sum_{\forall k\in\mathcal{K}} \frac{P_{\mathrm{AP}}\beta_0 F(\psi_{i,0})\beta_k F(\psi_{i,k})\left|\mathbf{g}_{i,k}^H\mathbf{\Theta}_i\mathbf{h}_i\right|^2}{\sigma_k^2}, \tag{32a}$$

$$\text{s.t. (31b).}$$

Algorithm 3 Iterative AO Algorithm

Input: Set iteration number $e = 0$, maximum number of iterations $E_{\max}$, and and initialize the coordinates $P_{\text{AP}} = P_{\text{AP}}^0$, $\boldsymbol{\Psi}_e = \boldsymbol{\Psi}_e^0$, $\boldsymbol{\beta}_e = \boldsymbol{\beta}_i^0$, $\boldsymbol{\Theta}_e = \boldsymbol{\Theta}_e^0$.

repeat

Solve problem (32) for given $\{\boldsymbol{\Psi}_i^{e-1}, \boldsymbol{\beta}_i^{e-1}, \boldsymbol{\Theta}_i^{e-1}\}$ and obtain the optimal P_{AP}^e.

Solve problem (33) for given $\{P_{\text{AP}}^{e-1}, \boldsymbol{\Psi}_i^{e-1}, \boldsymbol{\Theta}_i^{e-1}\}$ and obtain the optimal $\boldsymbol{\beta}_i^e$.

Solve problem (35) for given $\{P_{\text{AP}}^{e-1}, \boldsymbol{\beta}_i^{e-1}\}$ and obtain the sub-optimal $\{\boldsymbol{\Psi}_i^e, \boldsymbol{\Theta}_i^e\}$.

until e = $E_{\max}$

return $\{P_{\text{AP}}^*, \boldsymbol{\Psi}_i^*, \boldsymbol{\beta}_i^*, \boldsymbol{\Theta}_i^*\}$=$\{P_{\text{AP}}^e, \boldsymbol{\Psi}_i^e, \boldsymbol{\beta}_i^e, \boldsymbol{\Theta}_i^e\}$

It can be easily demonstrated that the optimization problem (16) is both affine and convex. This enables us to leverage the principles of convex optimization to find solutions. One approach involves differentiating the objective function with respect to P_{AP}, the transmit power of the AP. By equating this first-order derivative to zero while considering the constraint that limits the maximum transmit power, we can deduce the optimal solution as $P_{\text{AP}} = \max\{0, P_{\text{AP}}^{\max}\}$.

3.3.2 IRS Optimal Placement

In this subsection, we outline the subproblem in which the placement of the IRSs is optimized, with the IRS phase shift and radiation pattern held fixed, i.e., when $\boldsymbol{\Psi}_i$ and $\boldsymbol{\Theta}_i$ are known, and the optimal AP transmit power obtained from the previous sub-problem. Consequently, the optimization problem for determining each IRS central position can be formulated as follows:

$$\text{P}_7 : \max_{\boldsymbol{s}^i[n]} \sum_{\forall k \in \mathcal{K}} \frac{c_0^2 F(\psi_{i,0}) F(\psi_{i,k}) \left|\mathbf{g}_{i,k}^H \boldsymbol{\Theta}_i \mathbf{h}_i\right|^2}{\sigma_k^2 \|\boldsymbol{s}^i[n] - \boldsymbol{a}\|^{\alpha_0} \|\boldsymbol{s}^i[n] - \boldsymbol{u}[n,k]\|^{\alpha_k}}, \tag{33a}$$

$$\text{s.t. (31d).}$$

In this formulation, the $\boldsymbol{\beta}_i$'s are replaced by the IRSs' location decision variables, $\boldsymbol{s}^i[n]$. Notably, it is evident that the optimization problem (17) is convex in nature, facilitating the determination of an optimal solution. By equating the first-order derivative of the objective function with respect to $\boldsymbol{s}^i[n]$ to zero while taking into account the maximum SNR, we derive the following quality:

$$\frac{\left(a_\triangle - s_\triangle^i[n]\right)}{\left(a_x - s_x^i[n]\right)^2 + \left(a_y - s_y^i[n]\right)^2 + \left(a_z - s_z^i[n]\right)^2} = \frac{\left(s_\triangle^i[n] - u_\triangle[n,k]\right)}{\left(s_x^i[n] - u_y[n,k]\right)^2 + \left(s_y^i[n] - u_y[n,k]\right)^2 + \left(s_z^i[n] - u_z[n,k]\right)^2}, \quad \forall \triangle \in x, y, z,\ \forall k \in \mathcal{K},\ \forall i \in \mathcal{I},\ \forall n \in \mathcal{N}, \tag{34}$$

We can observe (34) gives each IRS's central position in the 3D coordinates where it is assumed $\alpha_k = 2$ to achieve these closed-from solutions [23].

Now, an iterative approach can be employed to determine the optimal IRSs' position. Beginning with predefined or initial values for $s_x^i[n]$, $s_y^i[n]$, and $s_z^i[n]$, the optimal x-coordinate, y-coordinate and z-coordinate of the IRS are computed iteratively using (34) while adhering to constraint 31d. This iterative refinement process converges to optimize the IRS's placement within the 3D plane, driven by the system's performance metric and constraints.

3.3.3 Passive Beamforming and Radiation Pattern Optimization at the IRS

We now consider the subproblem of jointly optimizing $\boldsymbol{\Psi}_i$ and $\boldsymbol{\Theta}_i$ with fixed P_{AP} and $\boldsymbol{\beta}_i$, which can be given by:

$$\mathrm{P}_8 : \max_{\boldsymbol{\Psi}_i, \boldsymbol{\Theta}_i} \ \gamma_{i,k}(\boldsymbol{\Psi}_i, \boldsymbol{\Theta}_i), \tag{35a}$$

$$\text{s.t. (31c).} \tag{35b}$$

Unlike the previous two subproblems, which have closed-form solutions, finding closed-form solutions for $\boldsymbol{\Psi}_i$ and $\boldsymbol{\Theta}_i$ is a challenging task, primarily because of the constraints related to the unit modulus of the IRS elements. Fortunately, we can employ successive convex approximation methods to convert the rank unit modulus constraint into linear matrix inequalities in each iteration, as described in [15] to find a sub-optimal solution. The Final iterative-based AO algorithm is provided in **Algorithm** 3.

3.4 Computational Complexity and Convergence Analysis

In this section, we conduct a comprehensive analysis of the computational complexity associated with our proposed algorithm, as referenced in [16]. This exploration is crucial for understanding the practical applicability and efficiency of the design resource allocation algorithm.

Initially, we examine the optimization problem P_6 (32). This problem is distinguished by its convex nature, enabling efficient resolution within a polynomial time complexity order. Characterized by a singular optimization variable coupled with one convex constraint, the computational complexity for each iteration maintains a constant order, denoted as:

$$O_1 = \mathcal{O}(1). \tag{36}$$

Moving forward to optimization problem P_7 (33), we encounter a scenario of increased complexity. This convex problem is defined by $3IN$ decision variables and an equal number of constraints, reflecting a significant expansion in computational demands compared to P_6 (32). Consequently, the complexity for this segment is approximated as:

$$O_2 \approx \mathcal{O}((IN)^4), \tag{37}$$

indicating a quartic relationship with the product of the number of IRSs I and the number of UEs N. This polynomial increase emphasizes the computational intensity required as the problem dimensions expand.

Further complexity unfolds with the reformulation of equation P_8 (35) into an SDP. The computational intricacy of an SDP, featuring w SDP constraints and engaging a positive semi-definite matrix of dimensions $v \times v$ is give by:

$$O_3 = \mathcal{O}\left(\sqrt{v}\log(1/\zeta)(wv^3 + w^2v^2 + w^3)\right). \tag{38}$$

Here, $\zeta > 0$ epitomizes the precision of the solution, as expounded in [15]. This expression highlights the subtle trade-off between matrix size, constraint volume, and desired accuracy in shaping computational workload.

The overall complexity of the proposed algorithmic solution is thus a function of the complexities of solving optimizing problems (16), (17), and (21). This yields an aggregate complexity of:

$$\mathcal{O}_{\text{tot}} = \mathcal{O}(e_{\text{iter}}(O_1 + O_2 + O_3)), \tag{39}$$

offering a comprehensive overview of the computational demands of the algorithm across both stages of optimization. The overall complexity in $\mathcal{O}_{\text{tot}}$ is an order four polynomial, where e_{iter} signifies the iteration count necessary for the AO iterative algorithm to achieve convergence.

In the following, we also prove that our algorithm is convergent.

Proposition 1 *The objective function value of P_5 would be improved via this iterative algorithm.*

Proof 1 *Let us consider $\{P_{\text{AP}}^{(j)}, \boldsymbol{\Psi}_i^{(j)}, \boldsymbol{\beta}_i^{(j+1)}, \boldsymbol{\Theta}_i^{(j+1)}\}$ as the feasible solution set to P_8. Then, the feasible solution set of P_8 is a feasible solution to P_5 as well. Therefore, $\{P_{\text{AP}}^{(j)}, \boldsymbol{\Psi}_i^{(j)}, \boldsymbol{\beta}_i^{(j)}, \boldsymbol{\Theta}_i^{(j)}\}$ and $\{P_{\text{AP}}^{(j+1)}, \boldsymbol{\Psi}_i^{(j+1)}, \boldsymbol{\beta}_i^{(j)}, \boldsymbol{\Theta}_i^{(j)}\}$ are feasible to P_5 in the (j)-th and $(j+1)$- th iterations, respectively.*

Now, we define $f_{P_5}(P_{\rm AP}^{(j)}, \boldsymbol{\Psi}_i^{(j)}, \boldsymbol{\beta}_i^{(j)}, \boldsymbol{\Theta}_i^{(j)})$, $f_{P_8}(\boldsymbol{\beta}_i^{(j)}, \boldsymbol{\Theta}_i^{(j)})$, $f_{P_7}(\boldsymbol{\Psi}_i^{(j)})$, and $f_{P_6}(P_{\rm AP}^{(j)})$ as the objective functions of problem P_5, P_8 and P_6 in the (j)-th iteration, respectively. Thus, we have

$$
\begin{aligned}
& f_{P_5}(P_{\rm AP}^{(j+1)}, \boldsymbol{\Psi}_i^{(j+1)}, \boldsymbol{\beta}_i^{(j+1)}, \boldsymbol{\Theta}_i^{(j+1)}) \\
& \overset{(a)}{=} f_{P_8}(\boldsymbol{\beta}_i^{(j+1)}, \boldsymbol{\Theta}_i^{(j+1)}) \overset{(b)}{\geq} f_{P_8}(\boldsymbol{\beta}_i^{(j)}, \boldsymbol{\Theta}_i^{(j)}) \\
& = f_{P_5}(P_{\rm AP}^{(j)}, \boldsymbol{\Psi}_i^{(j)}, \boldsymbol{\beta}_i^{(j)}, \boldsymbol{\Theta}_i^{(j)}),
\end{aligned} \tag{40}
$$

where (a) follows the fact that problem P_5 is equivalent to problem P_8 for optimal $P_{\rm AP}$ and $\boldsymbol{\Psi}_i$, and (b) holds since $f_{P_8}(\boldsymbol{\beta}_i^{(j+1)}, \boldsymbol{\Theta}_i^{(j+1)}) \geq f_{P_8}(\boldsymbol{\beta}_i^{(j)}, \boldsymbol{\Theta}_i^{(j)})$ according to sub-problem 3 (that is, optimizing passive beamforming and radiation pattern optimization at the IRS). Similarly, for a given $P_{\rm AP}^{(j)}, \boldsymbol{\beta}_i^{(j)}, \boldsymbol{\Theta}_i^{(j)}$, we have

$$
\begin{aligned}
& f_{P_5}(P_{\rm AP}^{(j+1)}, \boldsymbol{\Psi}_i^{(j+1)}, \boldsymbol{\beta}_i^{(j+1)}, \boldsymbol{\Theta}_i^{(j+1)}) \\
& \overset{(a)}{=} f_{P_7}(\boldsymbol{\Psi}_i^{(j+1)}) \overset{(b)}{\geq} f_{P_7}(\boldsymbol{\Psi}_i^{(j)}) \\
& = f_{P_5}(P_{\rm AP}^{(j)}, \boldsymbol{\Psi}_i^{(j)}, \boldsymbol{\beta}_i^{(j)}, \boldsymbol{\Theta}_i^{(j)}).
\end{aligned} \tag{41}
$$

where (a) follows the fact that problem P_5 is equivalent to problem P_7 for optimal $P_{\rm AP}, \boldsymbol{\beta}_i$, and $\boldsymbol{\Theta}_i$, and (b) holds since $f_{P_7}(\boldsymbol{\Psi}_i^{(j+1)}) \geq f_{P_7}(\boldsymbol{\Psi}_i^{(j)})$ according to sub-problem 2 (that is, the IRS optimal placement). Equivalently, for a given $\boldsymbol{\Psi}_i^{(j)}, \boldsymbol{\beta}_i^{(j)}, \boldsymbol{\Theta}_i^{(j)}$, we have

$$
\begin{aligned}
& f_{P_5}(P_{\rm AP}^{(j+1)}, \boldsymbol{\Psi}_i^{(j+1)}, \boldsymbol{\beta}_i^{(j+1)}, \boldsymbol{\Theta}_i^{(j+1)}) \\
& \overset{(a)}{=} f_{P_6}(P_{\rm AP}^{(j+1)}) \overset{(b)}{\geq} f_{P_6}(P_{\rm AP}^{(j)}) \\
& = f_{P_5}(P_{\rm AP}^{(j)}, \boldsymbol{\Psi}_i^{(j)}, \boldsymbol{\beta}_i^{(j)}, \boldsymbol{\Theta}_i^{(j)}).
\end{aligned} \tag{42}
$$

where (a) follows the fact that problem P_5 is equivalent to problem P_6 for optimal $\boldsymbol{\Psi}_i, \boldsymbol{\beta}_i$, and $\boldsymbol{\Theta}_i$, and (b) holds since $f_{P_6}(P_{\rm AP}^{(j+1)}) \geq f_{P_6}(P_{\rm AP}^{(j)})$ according to sub-problem 1 (that is, the AP transmit power control). From the above three inequalities, we can conclude the following inequality holds

$$
f_{P_5}(P_{\rm AP}^{(j+1)}, \boldsymbol{\Psi}_i^{(j+1)}, \boldsymbol{\beta}_i^{(j+1)}, \boldsymbol{\Theta}_i^{(j+1)}) \geq f_{P_5}(P_{\rm AP}^{(j)}, \boldsymbol{\Psi}_i^{(j)}, \boldsymbol{\beta}_i^{(j)}, \boldsymbol{\Theta}_i^{(j)}). \tag{43}
$$

Thus, we have shown that the objective function of P_5 is monotonically non-decreasing after each iteration. ■

Table 1: Baseline simulation parameters for communication and active sensing tasks

Parameter Name	**Parameter Value**
Application Type	OnOffApplication
Data Rate	150 Mbps
Flow Direction	Downlink
Payload Size	1448 Bytes
Transport Protocol	UDP
MAC Queue Size	4000 Packets
Aggregation Type	A-MSDU and A-MPDU
MAC / PHY	CSMA/CA / SC DMG MCS-10
Transmit Power / Sectors	10 mW / 8
Rx Noise Figure	10 dB
Operating Frequency	60.48 GHz

4 Context-Aware IRS Utilization Performance

4.1 Evaluation Setup

We utilize a simulation framework for assessing the performance of the AO algorithm in an IRS-assisted full-immersive VR-supporting mmWave network, accounting for the locations of the HMDs, the AP, and the IRS within a 3D setting. The allocation of IRS resources is considered within the environment's outer walls, excluding floor and ceiling. The AP is centered on the ceiling at 3 m height with the HMDs navigating in environments sized 10×10, 15×15, or 20×20 m^2, reflecting future deployment site configurations [42].

The proposed AO algorithm is derived for a generic number of IRS elements, where the allocation of the number of such resources will depend on the communication data-rate requirements of the future VR systems. In the instantiation of our approach, we consider 200 such elements, each of them sized $\lambda/5$ [32, 33]. We utilize the discrete-event network simulator (ns-3) simulator, in particular its WiGig module, which facilitates the analysis of the IEEE 802.11ad/ay protocols' performance [3]. Moreover, we incorporated a mmWave propagation model into the existing ns-3 framework that models the presence of IRSs on the signal propagation the environment. The summary of relevant simulation parameters is given in Table 2.

We designed two experiences in unbound VEs as shown in Figure 5. In multiuser VR setups, three different types of user coexistence can be distinguished: i) the users sharing solely the tracking space, ii) the users sharing only the VE, iii) the users sharing both the tracking space and VEs. In this study, both of the designed experiences abide to the first category. In the "straight path" experience, the users are assumed to follow a straight path during the full duration of the VE. This was considered as the worst case scenario given that the RDW algorithm was intuitively expected to have the most difficulties to unnoticeably redirect the users. In the "random path" experience, the users are assumed to immerse in an unbound VE and follow a randomly curved path. Hence, the curvature introduced by the RDW algorithm was expected to be less noticeable. Conceptually, the experiments consisted of the users walking in the unbound VEs while being confined to the restricted tracking space. The positional data of the users was utilized by the RDW algorithm to steer them inside the confined physical environment for collision avoidance. The physical walking trajectories for the two considered scenarios were generated utilizing the simulator from [21].

This study involves an extensive simulation where a user undertakes a virtual trajectory spanning approximately 6 minutes within an enclosed environment. As outlined above, the scenarios encompass the users traversing a linear, predetermined virtual pathway or navigating a randomly generated virtual trajectory. The simulation is orchestrated across varying UE density scenarios, specifically incorporating configurations involving one, two, or three UEs who concurrently walk throw the designated virtual environment.

The *"Optimal"* approach follows Algorithm 3 for dynamically adjusting IRS configuration and resources allocation based on the HMD, AP, and IRS locations, and IRS radiation patterns. We further consider the IRS element allocation at a *"Random"* location, as well as at an *"Oracle"* location that identifies the IRS element allocation all potential locations across room walls with

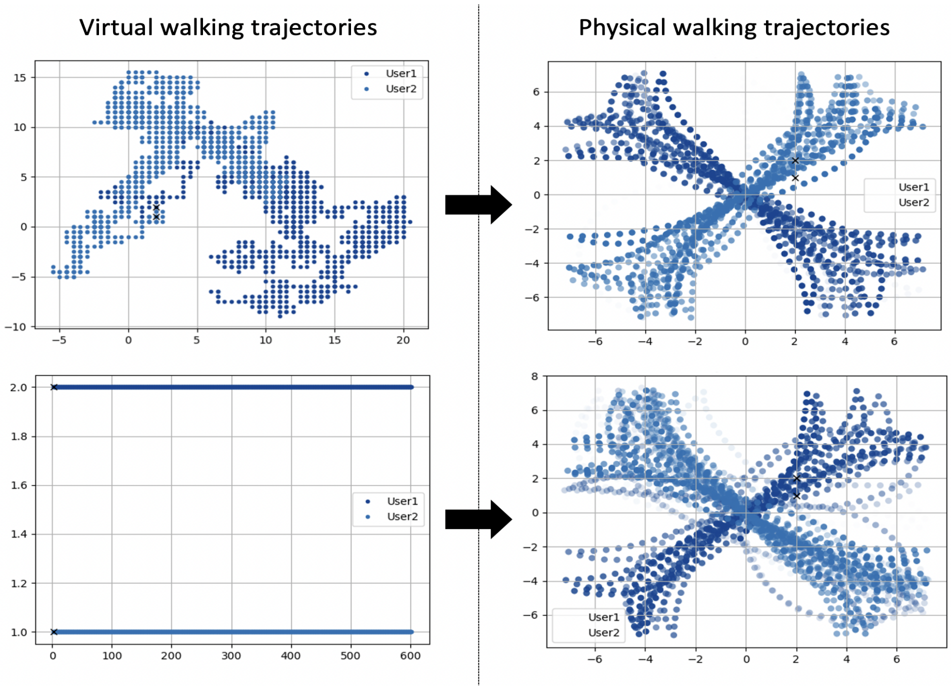

Figure 5: Physical and virtual path of two users when they follow a random or straight course in a VE

0.1 m-sized grid, and does that for every HMD location. Besides, the *"Best path"* is used to assess the performance of the combination of the direct AP-HMD and AP-IRS-HMD links, with IRS elements allocated utilizing the *"Optimal"* approach.

The modelling of passive sensing tasks is based on finding the UE's 3D imaging reconstruction and location by combining mmWave Frequency Modulated Continuous Wave (FMCW) signals with IRS positioning. FMCW signals exhibit a linear frequency change over time and can be mathematically described as:

$$m(t) = \cos\left(2\pi\left(f_c t + \frac{1}{2}Kt^2\right)\right), \quad 0 \leq t \leq T, \tag{44}$$

where f_c denotes the carrier frequency and $K = \frac{B}{T}$ represents the frequency slope. By leveraging the linear increase in frequency and the concept that time delay results in frequency shift, the Time of Flight (τ) can be estimated to then compute the distance to the target as $\tau = \frac{d_t(x,y,z)+d_{ri}(x,y,z)}{c}$. Taking into account the target reflectivity and round-trip decay, the received signal at the i^{th} Receiver can be expressed as:

$$Sb_i(x,y,z,t) = \alpha_i e^{j2\pi\frac{Kd_i(x,y,z)}{c}t}, \tag{45}$$

$$\alpha_i = \sigma_{0i} e^{j2\pi f_c \tau_i} \tag{46}$$

where α_i represents the attenuated amplitude from the i^{th} receiver in relation to the specified target, taking into account the distance and target reflectivity which in the evaluation setup is 0. It also contains the phase shift of the central frequency term.

As the objective is to reconstruct the user's 3D image, a single target or point reflector is insufficient. Therefore, the formulation needs to be expanded to account for multiple targets. The total received signal at the i^{th} receiver can be expressed as:

$$St_i(t) = \sum_{l=1}^{L} \alpha_{il} e^{j2\pi K\tau_{li}t} \tag{47}$$

where L represents the number of targets, that will depend on the the reflectivity of the points and their occlusion.

Table 2: Baseline simulation parameters for advanced sensing tasks

Parameter Name	**Parameter Value**
Transmit Power	10 mW
Rx Noise Figure	10 dB
Operating Frequency	77 GHz
Bandwidth	1.2 GHz
FMCW Sweep Time	0.8 ms
Sampling Rate	500 kHz
Number of IRS Elements	4000

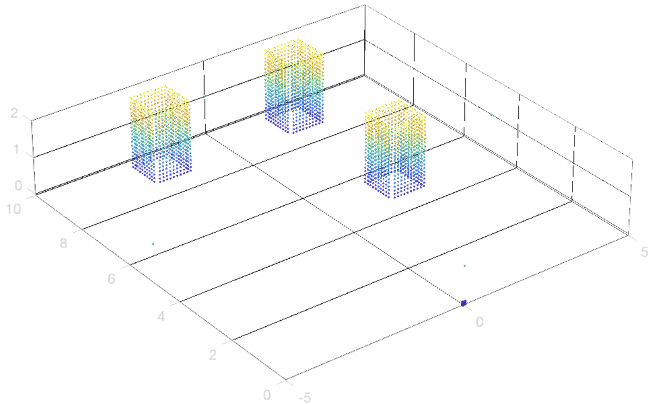

Figure 6: Model for advanced passive sensing of users' volumetric representations

To perform an exhaustive analysis and compare the homogeneity of the signal's SNR in different UE locations, we take into account an UE has 4 sides and can be modeled as a box (cf., Figure **??**) and the simulation setup is equipped with 4 different algorithms. Firstly we have the *"NoIRS"* environment in which we only consider the signal from the AP. Secondly, a *"Random"* one, that places the center of the IRS at a random position along its corresponding wall. Additionally, we employ the *"Exhaustive Search"* algorithm, which seeks the optimal coordinates for the IRS. This exhaustive search involves examining all the walls of the room for each UE position, with the consideration of 1000 IRS placements for each wall. Thus, when dealing with 3 UEs, this algorithm will output the optimal locations for 12 IRS units, as each UE has one associated with each wall. Finally, the module has an *"Optimal"* algorithm explained in *IRS Optimal Placement*, which efficiently finds a sub-optimal solution significantly faster than the Exhaustive method.

4.2 Evaluation Results

4.2.1 Communication and Active Sensing Coverage, and Active Sensing Accuracy

We evaluated the coverage of different approaches and expressed it through average throughput and its standard deviation against a maximum threshold of 150 Mbps, focusing on scenarios with a single and multiple HMD navigating through different environments (cf., Table 4). A snapshot of the results, focusing on the 15×15 m^2 environment, is depicted in Figure 7. The throughput in each environment peaks when the IRS is optimally positioned for each HMD, in comparison to scenarios without an IRS and with its resource allocation at a random location. IRS resource allocation an oracle location occasionally yields higher throughput, yet the AO algorithm can closely match its performance for the majority of HMD locations, despite its real-time-operating nature. Notably, the average throughput considering both optimal IRS path and the direct HMD-AP channel is highly comparable to the oracle. Analyzing standard deviation, performance of the network without an IRS shows higher throughput variability across environments compared to the scenarios with IRS support, even for its random resource allocation in the environment. Moreover, the *"Optimal"* location-based IRS resource allocation yielded by the AO approach, as well as its combination

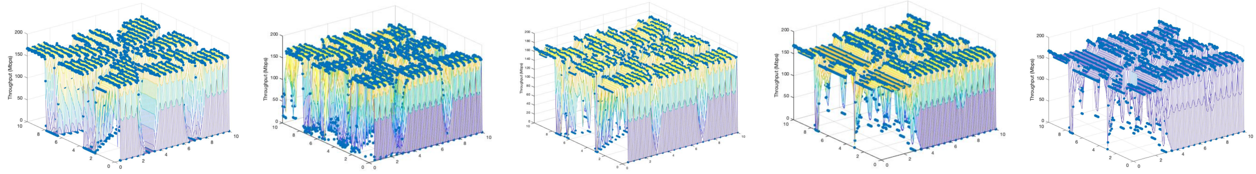

(a) No IRS (b) IRS at a random location (c) IRS at an optimal location (d) IRS at an oracle location (e) LoS + IRS at optimal

Figure 7: Communication coverage achieved by different approaches

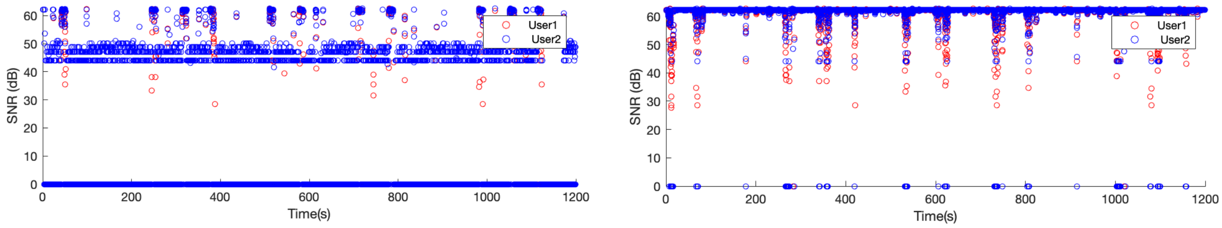

(a) 2 users, no IRS (b) 2 users, IRS at an optimal location

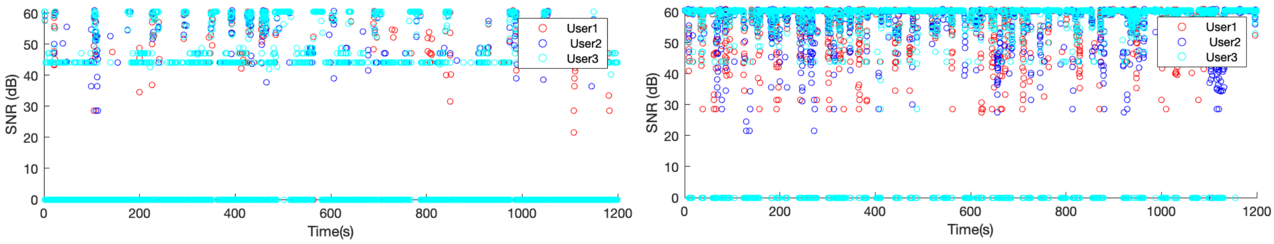

(c) 3 users, no IRS (d) 3 users, IRS at an optimal location

Figure 8: SNR variability enhancements due to the utilization of an IRS resources at location yielded by the proposed AO approach

with LoS communication, offer consistent throughput and low SNR variability, even in multiuser scenarios (cf., Figure 8).

4.2.2 Advanced Sensing Accuracy

This exploration entails a comprehensive analysis that encapsulates a spectrum of connectivity scenarios with diverse room dimensions. We have measured the average SNR and the Standard Deviation (SD) of this SNR to observe how performance in homogeneity increases in each scenario. These scenarios are conducted with the values of Table I, with 1, 2 and 3 users.

Table 4 presents the outcomes corresponding to the four specified scenarios in the evaluation setup, considering three different room sizes. The data for 1, 2, and 3 users are documented for each scenario. Each column, arranged from left to right, provides information on the Scenario, the number of users, the average Signal-to-Noise Ratio (SNR) for 1 user, the average SNR for all users, the average standard deviation of SNR, and the standard deviation of the averaged SNRs. It is noteworthy that the average SNR is computed by determining the SNR's Standard Deviation for the four sides of the User Equipment's (UE) box and subsequently averaging it. On the other hand, the 'SD SNR' column directly calculates the standard deviation of the four average SNRs, each pertaining to a side of the UE's box.

The optimal placement of the IRS significantly influences both the average standard deviation (SD) and the standard deviation of the averaged Signal-to-Noise Ratio (SNR) for each User Equipment (UE). In comparison to the 'NoIRS' and 'Random' scenarios, the exhaustive and optimal cases demonstrate substantially lower values for these metrics. For instance, in a 10x10 room, the Average SD ranges from 0.294 to 0.371 in the 'NoIRS' and 'Random' scenarios, while in the

Table 3: Summary of achieved results

Approach	Room size [m]	Avg [Mbps]	SD [Mbps]
No IRS	10×10	$124,08$	$68,4051$
	15×15	$112,25$	$74,7407$
	20×20	$98,063$	$79,2939$
Random	10×10	$131,97$	$60,4667$
	15×15	$117,58$	$62,8617$
	20×20	$109,40$	$67,1633$
Optimal	10×10	$144,97$	$50,5537$
	15×15	$125,10$	$68,5524$
	20×20	$115,87$	$72,2035$
Oracle	10×10	$147,89$	$40,4191$
	15×15	$129,34$	$47,5146$
	20×20	$118,74$	$49,0862$
LoS + IRS optimal	10×10	$148,90$	$39,1131$
	15×15	$131,34$	$46,5221$
	20×20	$120,73$	$48,9770$

'Exhaustive' scenario, it hovers around 0.2, and in the 'Optimal' scenario, it is approximately 0.25. A more pronounced contrast emerges when examining the SD of the Averaged SNR (SD SNR). In the 'NoIRS' and 'Random' scenarios, this value is approximately 0.7 and 0.25 (respectively), whereas in the 'Exhaustive' scenario, it ranges from 0.018 to 0.117, and in the 'Optimal' scenario, it's around 0.11. These results can be seen clearly in TABLE II, showing the SNR for each side of the wall in the 10x10 room with 1 user. It is important to remark that the positioning of the IRS for $Wall_x$ only takes into account the side of the user's box completely parallel to it.

Table 4: UE's SNR coverage for each wall in 10x10

IRS	Wall 1	Wall 2	Wall 3	Wall 4	SD
No IRS	59,198	57,843	58,206	58,622	0,697
Random	58,206	58,442	57,957	58,79	0,2671
Exhaustive	56,501	56,487	56,527	56,684	0,091
Optimal	54,511	54,224	54,466	54,471	0,113

The optimization of homogeneity requires a loss in SNR. This decrease in SNR during exhaustive search and optimal placement is not uncommon and can be attributed to the granularity of the step used in IRS positioning. Occasionally, this granularity may lead to the selection of sub-optimal configurations. Additionally, to achieve homogeneity, the IRS positioning must adapt to the side with the smallest coverage, potentially sacrificing a potential SNR increase. Despite this, the decrease in SNR is needed in order to minimise the SD. The higher standard deviations in some scenarios imply increased fluctuations, potentially indicative of less reliable or consistent signal. Conversely, lower standard deviations signify more stability and consistency in the provided measurements across different room sizes.

Figure 4 illustrates the boxplots of SNR values within the confines of a 20x20 room. The initial five boxplots correspond to the 'NoIRS' scenario, with the first one representing the averaged SNR for the four walls. Subsequently, the following four boxplots depict the SNR for each wall of the UE. The subsequent five boxplots are associated with the 'Random' scenario, followed by those for the 'Exhaustive' scenario, and finally, for the 'Optimal' environment.

Observing the plots, it is evident that the variability in data for the first two scenarios is significantly larger, indicating less homogeneity and compactness. As previously noted, the SNR is higher in these scenarios. In contrast, the 'Optimal' and 'Exhaustive' scenarios showcase lower variability, with data appearing more compact. Although the SNR is slightly lower in these cases compared to the former, the trade-off becomes apparent in the low variability of data. The 'Exhaustive'

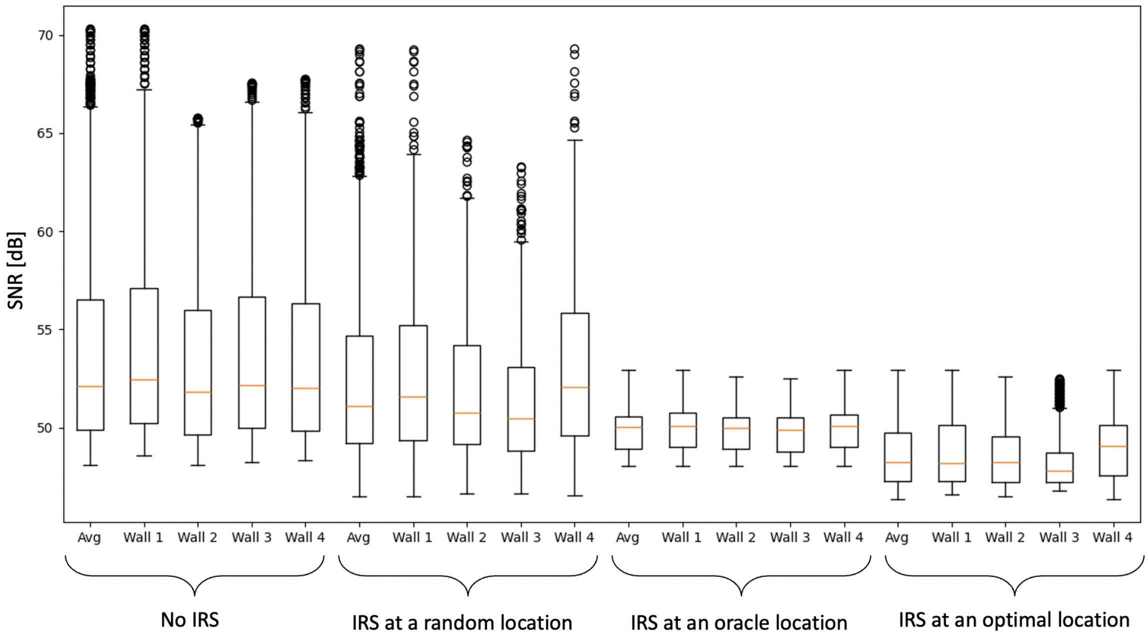

Figure 9: SNR distributions of different approaches in an 20x20 m^2 environment

solution yields superior SNR and variability compared to the 'Optimal' one, albeit at the expense of a significantly longer runtime—approximately 15 times slower in practice (without employing data parallelization).

Table 5: Coverage around UE

		10x10				15x15				20x20			
IRS	**U**	**SNRu**	**SNRt**	**Avg SD**	**SD SNR**	**SNRu**	**SNRt**	**Avg SD**	**SD SNR**	**SNRu**	**SNRt**	**Avg SD**	**SD SNR**
No IRS	1	58,415	58,415	0,283	0,697	54,306	54,306	0,171	0,451	53,415	53,415	0,197	0,488
	2	58.438	58,623	0,287	0,717	54,306	55,088	0,171	0,451	53,697	53,514	0,197	0,488
		58,809		0,324	0,696	55,869		0,247	0,586	53,331		0,165	0,462
	3	58,438	58,587	0,287	0,717	54,306	54,741	0,178	0,451	53,697	53,202	0,197	0,488
		58,809		0,324	0,696	55,869		0,247	0,586	53.331		0,165	0,462
		58,515		0,294	0,675	54,048		0,165	0,441	51,537		0,148	0,373
Random	1	58,198	58,198	0,331	0,2671	54,571	54,571	0,201	0,649	51,998	51,998	0,135	0,656
	2	58,201	58,209	0,318	0,241	54,674	54,691	0,207	0,505	52,031	52,048	0,137	0,667
		58,218		0,344	0,341	54,707		0,214	0,267	52,067		0,131	0,801
	3	58,137	58,235	0,321	0,171	54,674	54,718	0,206	0,49	52,009	51,853	0,136	0,595
		58,401		0,371	0,309	54,826		0,233	0,384	52,012		0,129	0,693
		58,166		0,332	0,317	54,654		0,203	0,883	51,537		0,132	1,199
Exhaustive	1	56,505	56,505	0,206	0,091	52,688	52,688	0,138	0.211	49,859	49,859	0,102	0,1255
	2	56,564	56,492	0,197	0,0185	52,688	52,438	0,138	0,211	49,864	49,915	0,1102	0,125
		56,421		0,202	0,065	52,188		0,144	0,108	50,005		0,103	0,193
	3	56,564	56,503	0,197	0,021	52,688	52,515	0,131	0,211	49,825	49,922	0,102	0,125
		56,421		0,202	0,065	52,188		0,144	0,108	530,005		0,103	0,193
		56,525		0,213	0,117	52,668		0,132	0,036	49,935		0,094	0,117
Optimal	1	54,866	54,866	0,253	0,113	51,213	51,213	0,166	0,289	48,63	48,63	0,125	0,261
	2	55,534	55,049	0,244	0,118	51,772	51,409	0,165	0,241	48,803	48,781	0,124	0,266
		54,561		0,254	0,108	51,046		0,166	0,225	48,756		0,126	0,243
	3	55,534	55,049	0,244	0,118	51,772	51,251	0,165	0,241	48,803	48,717	0,124	0,266
		54,561		0,254	0,108	51,046		0,166	0,225	48,756		0,126	0,243
		55,341		0,263	0,195	51,061		0,163	0,276	48,592		0,124	0,301

5 Conclusions, Future Directions, and Implications

- Summarizing key findings and insights from the chapter.
- Significance of the approach in overcoming technical limitations and maximizing the VR potential.
- Discussing potential future advancements in the field of VR communication and sensing.
- Exploring the broader implications of the proposed framework for the evolution of VR technologies.

In this article, we have presented a new AO algorithm that calculates the optimal placement of the centre position of an IRS depending on the UE and AP location inside and close environment. This AO algorithm is used as a new approach to improve VR performance by implementing the IRS on the room walls. This new approach is tested using the ns-3 network simulator, where we have included a module that incorporates the IRS at the end-to-end communication end. This new module has also combined the AO algorithm to optimise the IRSs' placement. The simulation results illustrated the advantages of implementing the IRS in future fully-immersed virtual reality environments and the efficacy of our proposed algorithm. These results show the improvement of the SNR and the extension of signal coverage achieved when implementing the IRS, in its optimal position, and the amount of items used by the IRS is adequate.

Acknowledgements

This work was supported by the Spanish Ministry of Economic Affairs and Digital Transformation and the European Union – NextGeneration EU, in the framework of the Recovery Plan, Transformation and Resilience (Call UNICO I+D 5G 2021, ref. number TSI-063000-2021-7); the European Union's Horizon Europe's research and innovation programme under grant agreement nº 101139161 — INSTINCT project; and MCIN / AEI / 10.13039 / 501100011033 / FEDER / UE HoloMit 2.0 project (nr. PID2021-126551OB-C21).

References

[1] Omid Abari, Dinesh Bharadia, Austin Duffield, and Dina Katabi. "Enabling {high-quality} untethered virtual reality". In: *14th USENIX Symposium on Networked Systems Design and Implementation (NSDI 17)*. 2017, pp. 531–544.

[2] Mohammed Almekhlafi, Mohamed Amine Arfaoui, Mohamed Elhattab, Chadi Assi, and Ali Ghrayeb. "Joint Resource Allocation and Phase Shift Optimization for RIS-Aided eMBB/URLLC Traffic Multiplexing". In: *IEEE Transactions on Communications* 70.2 (2022), pp. 1304–1319. DOI: 10.1109/TCOMM.2021.3127265.

[3] Vladislav Angelov, Emiliyan Petkov, Georgi Shipkovenski, and Teodor Kalushkov. "Modern virtual reality headsets". In: *2020 International congress on human-computer interaction, optimization and robotic applications (HORA)*. IEEE. 2020, pp. 1–5.

[4] Eric R Bachmann, Eric Hodgson, Cole Hoffbauer, and Justin Messinger. "Multi-user redirected walking and resetting using artificial potential fields". In: *IEEE transactions on visualization and computer graphics* 25.5 (2019), pp. 2022–2031.

[5] Karl-Ludwig Besser and Eduard A Jorswieck. "Reconfigurable intelligent surface phase hopping for ultra-reliable communications". In: *IEEE Transactions on Wireless Communications* 21.11 (2022), pp. 9082–9095.

[6] Nabeel Nisar Bhat, Rafael Berkvens, and Jeroen Famaey. "Gesture Recognition with mmWave Wi-Fi Access Points: Lessons Learned". In: *2023 IEEE 24th International Symposium on a World of Wireless, Mobile and Multimedia Networks (WoWMoM)*. IEEE. 2023, pp. 127–136.

[7] Emil Björnson and Luca Sanguinetti. "Power Scaling Laws and Near-Field Behaviors of Massive MIMO and Intelligent Reflecting Surfaces". In: *IEEE Open Journal of the Communications Society* 1 (2020), pp. 1306–1324.

[8] Christina Chaccour, Mehdi Naderi Soorki, Walid Saad, Mehdi Bennis, and Petar Popovski. "Risk-based optimization of virtual reality over terahertz reconfigurable intelligent surfaces". In: *ICC 2020-2020 IEEE International Conference on Communications (ICC)*. IEEE. 2020, pp. 1–6.

[9] Mingzhe Chen, Walid Saad, and Changchuan Yin. "Virtual reality over wireless networks: Quality-of-service model and learning-based resource management". In: *IEEE Transactions on Communications* 66.11 (2018), pp. 5621–5635.

[10] Johannes Dichgans and Thomas Brandt. "Visual-vestibular interaction: Effects on self-motion perception and postural control". In: *Perception*. Springer, 1978, pp. 755–804.

[11] Mohammed S Elbamby, Cristina Perfecto, Mehdi Bennis, and Klaus Doppler. "Toward low-latency and ultra-reliable virtual reality". In: *IEEE Network* 32.2 (2018), pp. 78–84.

[12] Jeff Feasel, Mary C Whitton, and Jeremy D Wendt. "LLCM-WIP: Low-latency, continuous-motion walking-in-place". In: *2008 IEEE symposium on 3D user interfaces*. IEEE. 2008, pp. 97–104.

[13] Shiqi Gong, Chengwen Xing, Pingyue Yue, Lian Zhao, and Tony Q. S. Quek. "Hybrid Analog and Digital Beamforming for RIS-Assisted mmWave Communications". In: *IEEE Transactions on Wireless Communications* 22.3 (2023), pp. 1537–1554. DOI: 10.1109/TWC.2022.3205322.

[14] Xiaoling Hu, Chenxi Liu, Mugen Peng, and Caijun Zhong. "IRS-Based Integrated Location Sensing and Communication for mmWave SIMO Systems". In: *IEEE Transactions on Wireless Communications* 22.6 (2023), pp. 4132–4145.

[15] Jalal Jalali, Ata Khalili, Atefeh Rezaei, Rafael Berkvens, Maarten Weyn, and Jeroen Famaey. "IRS-Based Energy Efficiency and Admission Control Maximization for IoT Users With Short Packet Lengths". In: *IEEE Transactions on Vehicular Technology* 72.9 (2023), pp. 12379–12384. DOI: 10.1109/TVT.2023.3266424.

[16] Jalal Jalali, Filip Lemic, Hina Tabassum, Rafael Berkvens, and Jeroen Famaey. "Toward Energy Efficient Multiuser IRS-Assisted URLLC Systems: A Novel Rank Relaxation Method". In: *2023 IEEE Globecom Workshops (GC Wkshps)*. 2023, pp. 1354–1360. DOI: 10.1109/GCWkshps58843.2023.10464825.

[17] Zheng-Ming Jiang, Mohamed Rihan, Peichang Zhang, Lei Huang, Qijun Deng, Jihong Zhang, and Ehab Mahmoud Mohamed. "Intelligent reflecting surface aided dual-function radar and communication system". In: *IEEE Systems Journal* 16.1 (2021), pp. 475–486.

[18] Markus Lappe, Frank Bremmer, and Albert V van den Berg. "Perception of self-motion from visual flow". In: *Trends in cognitive sciences* 3.9 (1999), pp. 329–336.

[19] Filip Lemic, Sergi Abadal, Chong Han, Johann M Marquez-Barja, Eduard Alarcon, and Jeroen Famaey. "Localization in power-constrained terahertz-operating software-defined metamaterials". In: *Nano Communication Networks* 30 (2021), p. 100365.

[20] Filip Lemic, James Martin, Christopher Yarp, Douglas Chan, Vlado Handziski, Robert Brodersen, Gerhard Fettweis, Adam Wolisz, and John Wawrzynek. "Localization as a feature of mmWave communication". In: *2016 International Wireless Communications and Mobile Computing Conference (IWCMC)*. IEEE. 2016, pp. 1033–1038.

[21] Filip Lemic, Jakob Struye, and Jeroen Famaey. "User mobility simulator for full-immersive multiuser virtual reality with redirected walking". In: *Proceedings of the 12th ACM Multimedia Systems Conference*. 2021, pp. 293–299.

[22] Filip Lemic, Jakob Struye, Thomas Van Onsem, Jeroen Famaey, and Xavier Costa Perez. "Predictive Context-Awareness for Full-Immersive Multiuser Virtual Reality with Redirected Walking". In: *IEEE Commununications Magazine* 61.9 (2023), pp. 32–38.

[23] Guang-Hui Li, Dian-Wu Yue, and Si-Nian Jin. "Spatially Correlated Rayleigh Fading Characteristics of RIS-Aided mmWave MIMO Communications". In: *IEEE Communications Letters* 27.8 (2023), pp. 2222–2226. DOI: 10.1109/LCOMM.2023.3289959.

[24] Kangbai Li, Miao Cui, Guangchi Zhang, Qingqing Wu, Dong Li, and Jiguang He. "Robust Transmit and Reflect Beamforming Design for IRS-Assisted Offshore NOMA Communication Systems". In: *IEEE Transactions on Vehicular Technology* 73.1 (2024), pp. 783–798. DOI: 10.1109/TVT.2023.3305535.

[25] Renwang Li, Xiaodan Shao, Shu Sun, Meixia Tao, and Rui Zhang. "Beam scanning for integrated sensing and communication in IRS-aided mmwave systems". In: *2023 IEEE 24th International Workshop on Signal Processing Advances in Wireless Communications (SPAWC)*. IEEE. 2023, pp. 196–200.

[26] Hai-Lin Liu, Fangqing Gu, and Qingfu Zhang. "Decomposition of a Multiobjective Optimization Problem Into a Number of Simple Multiobjective Subproblems". In: *IEEE Transactions on Evolutionary Computation* 18.3 (2014), pp. 450–455. DOI: 10.1109/TEVC.2013.2281533.

[27] Dushyant Mehta, Srinath Sridhar, Oleksandr Sotnychenko, Helge Rhodin, Mohammad Shafiei, Hans-Peter Seidel, Weipeng Xu, Dan Casas, and Christian Theobalt. "Vnect: Real-time 3d human pose estimation with a single rgb camera". In: *Acm transactions on graphics (tog)* 36.4 (2017), pp. 1–14.

[28] Salman Mohebi, Mattia Lecci, Andrea Zanella, and Michele Zorzi. "The challenges of Scheduling and Resource Allocation in IEEE 802.11ad/ay". In: *2020 Mediterranean Communication and Computer Networking Conference (MedComNet)*. 2020, pp. 1–4.

[29] Luis Muñoz-Saavedra, Lourdes Miró-Amarante, and Manuel Domínguez-Morales. "Augmented and virtual reality evolution and future tendency". In: *Applied Sciences* 10.1 (2020), p. 322.

[30] Niels Christian Nilsson, Tabitha Peck, Gerd Bruder, Eri Hodgson, Stefania Serafin, Mary Whitton, Frank Steinicke, and Evan Suma Rosenberg. "15 years of research on redirected walking in immersive virtual environments". In: *IEEE computer graphics and applications* 38.2 (2018), pp. 44–56.

[31] Thomas Nitsche, Carlos Cordeiro, Adriana B. Flores, Edward W. Knightly, Eldad Perahia, and Joerg C. Widmer. "IEEE 802.11ad: directional 60 GHz communication for multi-Gigabit-per-second Wi-Fi [Invited Paper]". In: *IEEE Communications Magazine* 52.12 (2014), pp. 132–141.

[32] Konstantinos Ntontin, Dimitrios Selimis, Alexandros-Apostolos A Boulogeorgos, Antonis Alexandridis, Aris Tsolis, Vasileios Vlachodimitropoulos, and Fotis Lazarakis. "Optimal reconfigurable intelligent surface placement in millimeter-wave communications". In: *2021 15th European Conference on Antennas and Propagation (EuCAP)*. IEEE. 2021, pp. 1–5.

[33] Özgecan Özdogan, Emil Björnson, and Erik G Larsson. "Intelligent reflecting surfaces: Physics, propagation, and pathloss modeling". In: *IEEE Wireless Communications Letters* 9.5 (2019), pp. 581–585.

[34] R. S. Prasobh Sankar, Battu Deepak, and Sundeep Prabhakar Chepuri. "Joint Communication and Radar Sensing with Reconfigurable Intelligent Surfaces". In: *2021 IEEE 22nd International Workshop on Signal Processing Advances in Wireless Communications (SPAWC)*. 2021, pp. 471–475.

[35] Macey Ruble and Ismail Güvenç. "Wireless localization for mmWave networks in urban environments". In: *EURASIP journal on advances in signal processing* 2018.1 (2018), pp. 1–19.

[36] Prerna Saxena and AG Kothari. "Performance analysis of adaptive beamforming algorithms for smart antennas". In: *IERI Procedia* 10 (2014), pp. 131–137.

[37] Frank Steinicke, Gerd Bruder, Jason Jerald, Harald Frenz, and Markus Lappe. "Analyses of human sensitivity to redirected walking". In: *Proceedings of the 2008 ACM symposium on Virtual reality software and technology*. 2008, pp. 149–156.

[38] Frank Steinicke, Gerd Bruder, Jason Jerald, Harald Frenz, and Markus Lappe. "Estimation of detection thresholds for redirected walking techniques". In: *IEEE transactions on visualization and computer graphics* 16.1 (2009), pp. 17–27.

[39] Jakob Struye, Filip Lemic, and Jeroen Famaey. “Covrage: Millimeter-wave beamforming for mobile interactive virtual reality”. In: *IEEE Transactions on Wireless Communications* (2022).

[40] Pau Talarn, Bernat Ollé, Filip Lemic, Sergi Abadal, and Xavier Costa-Perez. “Real-time Generation of 3-Dimensional Representations of Static Objects using Small Unmanned Aerial Vehicles”. In: *Proceedings of the 29th Annual International Conference on Mobile Computing and Networking*. 2023, pp. 1–3.

[41] Wankai Tang, Ming Zheng Chen, Xiangyu Chen, Jun Yan Dai, Yu Han, Marco Di Renzo, Yong Zeng, Shi Jin, Qiang Cheng, and Tie Jun Cui. “Wireless Communications With Reconfigurable Intelligent Surface: Path Loss Modeling and Experimental Measurement”. In: *IEEE Transactions on Wireless Communications* 20.1 (2021), pp. 421–439.

[42] Thomas Van Onsem, Jakob Struye, Xavier Costa Perez, Jeroen Famaey, and Filip Lemic. “Toward Full-Immersive Multiuser Virtual Reality With Redirected Walking”. In: *IEEE Access* 11 (2023), pp. 24722–24736.

[43] Hong Wang, Chen Liu, Zheng Shi, Yaru Fu, and Rongfang Song. “On Power Minimization for IRS-Aided Downlink NOMA Systems”. In: *IEEE Wireless Communications Letters* 9.11 (2020), pp. 1808–1811. DOI: 10.1109/LWC.2020.2999097.

[44] Peilan Wang, Jun Fang, Xiaojun Yuan, Zhi Chen, and Hongbin Li. “Intelligent Reflecting Surface-Assisted Millimeter Wave Communications: Joint Active and Passive Precoding Design”. In: *IEEE Transactions on Vehicular Technology* 69.12 (2020), pp. 14960–14973. DOI: 10.1109/TVT.2020.3031657.

[45] Yu Wang, Ticao Zhang, Shiwen Mao, and Theodore (Ted) S. Rappaport. “Directional neighbor discovery in mmWave wireless networks”. In: *Digital Communications and Networks* 7.1 (2021), pp. 1–15. ISSN: 2352-8648.

[46] Qingqing Wu and Rui Zhang. “Intelligent Reflecting Surface Enhanced Wireless Network via Joint Active and Passive Beamforming”. In: *IEEE Transactions on Wireless Communications* 18.11 (2019), pp. 5394–5409. DOI: 10.1109/TWC.2019.2936025.

[47] Yongzhi Wu, Filip Lemic, Chong Han, and Zhi Chen. “Sensing integrated DFT-spread OFDM waveform and deep learning-powered receiver design for terahertz integrated sensing and communication systems”. In: *IEEE Transactions on Communications* 71.1 (2022), pp. 595–610.

[48] Zhouyuan Yu, Xiaoling Hu, Chenxi Liu, Mugen Peng, and Caijun Zhong. “Location Sensing and Beamforming Design for IRS-Enabled Multi-User ISAC Systems”. In: *IEEE Transactions on Signal Processing* 70 (2022), pp. 5178–5193. DOI: 10.1109/TSP.2022.3217353.

[49] Peijun Zhao, Chris Xiaoxuan Lu, Bing Wang, Niki Trigoni, and Andrew Markham. “Cubelearn: End-to-end learning for human motion recognition from raw mmwave radar signals”. In: *IEEE Internet of Things Journal* (2023).

[50] Anfu Zhou, Leilei Wu, Shaoqing Xu, Huadong Ma, Teng Wei, and Xinyu Zhang. “Following the Shadow: Agile 3-D Beam-Steering for 60 GHz Wireless Networks”. In: *IEEE INFOCOM 2018 - IEEE Conference on Computer Communications*. 2018, pp. 2375–2383.

[51] Yi Zhou, Cunhua Pan, Phee Lep Yeoh, Kezhi Wang, Zheng Ma, Branka Vucetic, and Yonghui Li. “Latency minimization for secure intelligent reflecting surface enhanced virtual reality delivery systems”. In: *IEEE Wireless Communications Letters* 11.9 (2022), pp. 1770–1774.